

# Isolating chirality-breaking SMEFT operators with Drell-Yan angular analysis

**Samuele Grossi,<sup>a,b</sup> Xu Li,<sup>a</sup> Lorenzo Rolla,<sup>a,b</sup> Riccardo Torre,<sup>a</sup>**

<sup>a</sup>*INFN, Sezione di Genova, Via Dodecaneso 33, I-16146 Genova, Italy*

<sup>b</sup>*Department of Physics, University of Genova, Via Dodecaneso 33, I-16146 Genova, Italy*

*E-mail:* [riccardo.torre@ge.infn.it](mailto:riccardo.torre@ge.infn.it), [samuele.grossi@ge.infn.it](mailto:samuele.grossi@ge.infn.it),  
[xu.li@ge.infn.it](mailto:xu.li@ge.infn.it), [lorenzo.rolla@ge.infn.it](mailto:lorenzo.rolla@ge.infn.it)

**ABSTRACT:** We present a comprehensive strategy to isolate the effect of a class of chirality-breaking interactions in the Standard Model Effective Field Theory (SMEFT) by exploiting Drell-Yan angular analysis and the violation of the Lam-Tung relation. Unlike most SMEFT interpretation of Drell-Yan measurements, dominated by growing-with-energy effects generated by the interference of SMEFT-induced and SM amplitudes, this method isolates operators that contribute only quadratically in the Wilson coefficients, allowing for an independent probe of non-interfering directions in the EFT parameter space. Denoting with  $v$  the electroweak vev, with  $\sqrt{s}$  the center-of-mass energy, and with  $\Lambda$  the scale of new physics, depending on the nature of the SMEFT operators, the non-interfering contributions to the amplitude generated by the chirality-breaking operators can be proportional to  $v\sqrt{s}/\Lambda^2$  or  $s/\Lambda^2$ . We argue that these two classes can be further distinguished by analyzing the angular observables of the lepton pair in the transverse momentum and in the invariant mass distribution of the lepton pair. We therefore present an analysis of the lepton-pair angular observables in both the transverse momentum and invariant mass distributions. Based on a precise estimate of the Standard Model contribution to the relevant observables for the  $pp \rightarrow l^+l^- + X$  process up to  $\mathcal{O}(\alpha_S^2)$ , we present realistic projections for the sensitivity of the LHC with  $300 \text{ fb}^{-1}$  and for the HL-LHC with  $3 \text{ ab}^{-1}$  to chirality-breaking interactions, demonstrating that angular observables provide an independent and clean handle on SMEFT effects, especially in regions where the Standard Model contribution is naturally suppressed thanks to the Lam-Tung relation. This analysis becomes crucial to go beyond single parameter global fits, since it helps breaking degeneracies with chirality preserving operators and to disentangle overlapping directions in the EFT parameter space.

---

## Contents

<b>1</b>	<b>Introduction</b>	<b>1</b>
<b>2</b>	<b>Angular coefficients and the <math>A_0 - A_2</math> observable</b>	<b>6</b>
2.1	Monte Carlo simulation and uncertainty estimation	10
<b>3</b>	<b>Experimental status</b>	<b>13</b>
<b>4</b>	<b>Standard Model predictions</b>	<b>15</b>
4.1	Transverse momentum distribution	15
4.2	Invariant mass distribution	16
<b>5</b>	<b>SMEFT predictions</b>	<b>18</b>
5.1	Lam-Tung relation breaking at $\mathcal{O}(\alpha_S^0)$	18
5.2	Lam-Tung relation breaking at $\mathcal{O}(\alpha_S)$	19
<b>6</b>	<b>Analysis and projected limits</b>	<b>20</b>
<b>7</b>	<b>Results and discussion</b>	<b>23</b>
<b>8</b>	<b>Conclusions</b>	<b>26</b>
<b>A</b>	<b>The Collins-Soper frame</b>	<b>28</b>
<b>B</b>	<b>Angular observables from spherical-harmonics</b>	<b>29</b>
<b>C</b>	<b>Differential cross-section and PDF integration</b>	<b>29</b>
<b>D</b>	<b>Cross-section vs <math>A_0 - A_2</math> bounds</b>	<b>31</b>
<b>E</b>	<b>Numerical tables</b>	<b>32</b>
<b>F</b>	<b>UV models sensitive to our analysis</b>	<b>41</b>

---

## Contents

### 1 Introduction

The Standard Model Effective Field Theory (SMEFT) is the proper tool to look for new physics (NP) in the absence of direct evidence of new particles. It offers a consistent framework, both in terms of symmetries and, when empowered by essential assumptions

on the ultraviolet (UV) structure of NP, of power counting, to parametrize the effects of heavy NP at energies accessible to existing and future colliders.

Even though, already at dimension six, the number of operators appearing in the SMEFT is extremely large (especially if no assumptions on the flavor structure are made), not all such operators contribute to all processes and observables. Instead, there are usually specific classes of operators, including just a few of them, that contribute to specific classes of observables in specific kinematic regions. This consideration, together with the observation that the more differential observables are, the more information they carry about the underlying physics, often allows one to disentangle the effects of different operators and remove degeneracies and flat directions in the SMEFT parameter space.

One of the most studied processes, with all its related observables, in the context of testing the electroweak sector of the SMEFT at colliders, is the inclusive Drell-Yan (DY) process,  $pp \rightarrow \ell^+ \ell^- + X$ , where  $\ell$  is a lepton, typically an electron or a muon, and  $X$  is any additional particle over which the cross-section is integrated. The reason for this interest in the DY process is multifold: first, this is the cleanest experimental channel that can be studied at hadron colliders; second, it offers a very large statistics at the LHC, with order billions of events collected at the end of the LHC and tens of billions at the HL-LHC; third, it is one of the best-known processes from the point of view of theoretical predictions, with  $\mathcal{O}(\alpha_S^3)$  [1–4] and  $\mathcal{O}(\alpha\alpha_S)$  [5–7] calculations available in the literature; finally, as we argue in the present paper, even being a simple two-body final state, DY can offer a wide spectrum of observables, in different kinematic regimes, that allow one to disentangle the effects of different SMEFT operators. This is the reason that made the DY process the prototype process in the context of the high energy precision program at hadron colliders [8]. In this paper, we aim to further develop this program in a direction that has only recently gained attention [9]: the possibility of constraining classes of dimension-6 operators that do not interfere with the SM by analyzing regions of phase space where the SM contribution is suppressed. We refer to this emerging direction as the “high-energy precision beyond interference” program.

We can identify a relatively large class of dimension-six operators that contributes to the DY process, through contact interactions involving two quarks and two leptons, through modified vertices of leptons and/or quarks with neutral electroweak gauge bosons and the Higgs, and through modified gauge bosons and Higgs propagators.

Following the classification outlined in Ref. [10], the so-called Warsaw basis, the full set of such operators is summarized in Table 1. Here the notation is the following:  $\varphi$  is the Higgs doublet,  $D_\mu$  is the covariant derivative acting on  $\varphi$ ,  $\ell$  and  $e$  are the left-handed lepton doublet and right-handed lepton singlet, respectively,  $q$  and  $u$  ( $d$ ) are the left-handed quark doublet and right-handed up (down) quark singlet, respectively,  $\tilde{\varphi} = i\sigma_2\varphi^*$  is the conjugate Higgs doublet,  $W_{\mu\nu}^I$  and  $B_{\mu\nu}$  are the field strength tensors of the  $SU(2)_L$  and  $U(1)_Y$  gauge groups, respectively, and  $\tau^I$  are the  $SU(2)_L$  generators in the fundamental representation. Furthermore, the indices  $p, r, s, t$  run over the different flavors of leptons and quarks, the lowercase indices  $j, k$  and the capital index  $I$  run over the fundamental and adjoint representations of  $SU(2)_L$ , respectively, and  $\epsilon_{jk}$  is the Levi-Civita symbol in two dimensions. Finally, we clarify that we refer to chirality-breaking operators as those

1. $\varphi^4 D^2$		2. $\psi^2 \varphi^3$	
$Q_{\varphi\Box}$	$(\varphi^\dagger \varphi) \Box (\varphi^\dagger \varphi)$	$Q_{e\varphi}$	$(\varphi^\dagger \varphi)(\bar{\ell}_p e_r \varphi)$
$Q_{\varphi D}$	$(\varphi^\dagger D^\mu \varphi)^* (\varphi^\dagger D_\mu \varphi)$	$Q_{u\varphi}$	$(\varphi^\dagger \varphi)(\bar{q}_p u_r \tilde{\varphi})$
		$Q_{d\varphi}$	$(\varphi^\dagger \varphi)(\bar{q}_p d_r \varphi)$
3. $\psi^2 X \varphi$		4. $\psi^2 \varphi^2 D$	
$Q_{eW}$	$(\bar{\ell}_p \sigma^{\mu\nu} e_r) \tau^I \varphi W_{\mu\nu}^I$	$Q_{\varphi l}^{(1)}$	$(\varphi^\dagger i \overleftrightarrow{D}_\mu \varphi)(\bar{\ell}_p \gamma^\mu \ell_r)$
$Q_{eB}$	$(\bar{\ell}_p \sigma^{\mu\nu} e_r) \varphi B_{\mu\nu}$	$Q_{\varphi l}^{(3)}$	$(\varphi^\dagger i \overleftrightarrow{D}_\mu \varphi)(\bar{\ell}_p \tau^I \gamma^\mu \ell_r)$
$Q_{uW}$	$(\bar{q}_p \sigma^{\mu\nu} u_r) \tau^I \tilde{\varphi} W_{\mu\nu}^I$	$Q_{\varphi e}$	$(\varphi^\dagger i \overleftrightarrow{D}_\mu \varphi)(\bar{e}_p \gamma^\mu e_r)$
$Q_{uB}$	$(\bar{q}_p \sigma^{\mu\nu} u_r) \tilde{\varphi} B_{\mu\nu}$	$Q_{\varphi q}^{(1)}$	$(\varphi^\dagger i \overleftrightarrow{D}_\mu \varphi)(\bar{q}_p \gamma^\mu q_r)$
$Q_{dW}$	$(\bar{q}_p \sigma^{\mu\nu} d_r) \tau^I \varphi W_{\mu\nu}^I$	$Q_{\varphi q}^{(3)}$	$(\varphi^\dagger i \overleftrightarrow{D}_\mu \varphi)(\bar{q}_p \tau^I \gamma^\mu q_r)$
$Q_{dB}$	$(\bar{q}_p \sigma^{\mu\nu} d_r) \varphi B_{\mu\nu}$	$Q_{\varphi u}$	$(\varphi^\dagger i \overleftrightarrow{D}_\mu \varphi)(\bar{u}_p \gamma^\mu u_r)$
		$Q_{\varphi d}$	$(\varphi^\dagger i \overleftrightarrow{D}_\mu \varphi)(\bar{d}_p \gamma^\mu d_r)$
		$Q_{\varphi ud}$	$i(\tilde{\varphi}^\dagger D_\mu \varphi)(\bar{u}_p \gamma^\mu d_r)$
5. $(\bar{L}L)(\bar{L}L)$		6. $(\bar{R}R)(\bar{R}R)$	
$Q_{lq}^{(1)}$	$(\bar{\ell}_p \gamma_\mu \ell_r)(\bar{q}_s \gamma^\mu q_t)$	$Q_{eu}$	$(\bar{e}_p \gamma_\mu e_r)(\bar{u}_s \gamma^\mu u_t)$
$Q_{lq}^{(3)}$	$(\bar{\ell}_p \gamma_\mu \tau^I \ell_r)(\bar{q}_s \gamma^\mu \tau^I q_t)$	$Q_{ed}$	$(\bar{e}_p \gamma_\mu e_r)(\bar{d}_s \gamma^\mu d_t)$
7. $(\bar{L}L)(\bar{R}R)$		8. $(\bar{L}R)(\bar{R}L)$ and $(\bar{L}R)(\bar{L}R)$	
$Q_{lu}$	$(\bar{\ell}_p \gamma_\mu \ell_r)(\bar{u}_s \gamma^\mu u_t)$	$Q_{ledq}$	$(\bar{\ell}_p^j e_r)(\bar{d}_s q_t^j)$
$Q_{ld}$	$(\bar{\ell}_p \gamma_\mu \ell_r)(\bar{d}_s \gamma^\mu d_t)$	$Q_{lequ}^{(1)}$	$(\bar{\ell}_p^j e_r) \epsilon_{jk} (\bar{q}_s^k u_t)$
$Q_{qe}$	$(\bar{q}_p \gamma_\mu q_r)(\bar{e}_s \gamma^\mu e_t)$	$Q_{lequ}^{(3)}$	$(\bar{\ell}_p^j \sigma_{\mu\nu} e_r) \epsilon_{jk} (\bar{q}_s^k \sigma^{\mu\nu} u_t)$

**Table 1:** Operators contributing to the Drell-Yan process in the Warsaw basis. The notation is the same as in Ref. [10]. The operators are grouped according to their field content and the first column indicates the operator's name.

higher dimensional interaction terms that are not invariant under a  $SU(N_f)_L \times SU(N_f)_R$  transformation, with  $N_f$  the number of flavors of the SM and  $SU(N_f)_L$  ( $SU(N_f)_R$ ) acting non trivially only on left-handed (right-handed) spinors.

Despite, as anticipated, the number of operators that may contribute to the DY process at hadron colliders is rather large, their behavior can be very different, depending on the kinematic region. It is useful to classify them according to two main features: the first is whether they contribute at the linear or at the quadratic level (*i.e.* whether they interfere with the Standard Model (SM) amplitude or not), the second is their behavior with respect to the energy of the process, *i.e.* whether they lead to amplitudes that grow with energy or not. Indeed, we generally expect the following different contributions the amplitude:

$$\frac{v^2}{\Lambda^2}, \quad \frac{v\sqrt{s}}{\Lambda^2}, \quad \frac{s}{\Lambda^2}. \quad (1.1)$$

Let us comment the different operator classes in turn.

- **1.  $\varphi^4 D^2$**

The operators in this class modify the Higgs and gauge boson propagators on-shell,

generating corrections to their kinetic terms suppressed by  $v^2/\Lambda^2$ . The Drell-Yan amplitude involving these operators is proportional to  $v^2/\Lambda^2$ , leading to an interference with the SM amplitude proportional to  $v^2/\Lambda^2$ , and to a contribution to the squared amplitude proportional to  $v^4/\Lambda^4$ . These contributions do not grow with energy, and are therefore better constrained in very precise experiments at the threshold for on-shell production of SM bosons (such as LEP or future lepton colliders).

- **2.  $\psi^2\varphi^3$**

These operators are  $v^2/\Lambda^2$  corrections to the Yukawa couplings of the SM. Obviously, their flavor structure may determine stronger or weaker bounds from flavor physics. However, their contribution to the DY amplitude is proportional to  $v^2/\Lambda^2$  and not enhanced with the energy. We can therefore neglect the contribution of these operators to the DY process.

- **3.  $\psi^2 X \varphi$**

This class of operators contains dipole interactions between fermions and gauge bosons. Some combinations of these operators, such as those leading to electron dipole moments, are very strongly constrained by low-energy experiments. However, as we will see, other combinations can effectively be constrained from DY measurements. Indeed, the contribution of these chirality-breaking operators to the DY amplitude is proportional to  $v\sqrt{s}/\Lambda^2$ . Due to the chirality structure of the fermionic tensor, the DY amplitude generated by these operators does not interfere with the SM amplitude. Therefore, their contribution to the squared amplitude scales as  $v^2 s/\Lambda^4$ , growing linearly with  $s$ .

- **4.  $\psi^2\varphi^2 D$**

These operators have the form of product of a fermion and a Higgs current. They lead to a  $v^2/\Lambda^2$  corrections to the interactions of fermions with gauge bosons and the Higgs. Their contribution to the DY amplitude does interfere with the SM ones, but does not grow with energy, generating terms proportional to  $v^2/\Lambda^2$  and  $v^4/\Lambda^4$  in the squared amplitude. As for the operators of class 1, these contributions are better constrained in precise experiments at the threshold for on-shell production of SM bosons.

- **5.  $(\bar{L}L)(\bar{L}L)$ , 6.  $(\bar{R}R)(\bar{R}R)$ , 7.  $(\bar{L}L)(\bar{R}R)$**  The seven operators in these classes correspond to the product of two fermion currents. They are the only operators that lead to contributions to the DY amplitude that are proportional to  $s/\Lambda^2$ , and, at the same time, interfere with the SM amplitudes. Therefore, they generate contributions to the squared amplitude proportional to  $s/\Lambda^2$  and  $s^2/\Lambda^4$ . These operators have been extensively studied in the context of the DY process at the LHC [8, 11–14].

- **8.  $(\bar{L}R)(\bar{R}L)$  and  $(\bar{L}R)(\bar{L}R)$**

The last class of operators contains chirality-breaking interactions of two scalar or two tensor fermion bilinears. We will refer to them as “scalar” and “tensor” four-fermion operators, respectively. Their contribution to the DY amplitude has the

same energy behavior of the current-current four-fermion operators.<sup>1</sup> However, due to the chirality structure of the fermionic tensors, they do not interfere with the SM amplitude, leading to contributions to the squared amplitude that are proportional to  $s^2/\Lambda^4$ . These operators, together with those in class 3, can be constrained by DY measurements, and will constitute the main focus of the present paper. In the following, we denote them as  $\psi_{(8)}^4$ .

Summarizing, operators in classes 1, 2, and 4 lead to contributions to the DY amplitude that do not grow with energy and are therefore better constrained in experiments at the SM boson production threshold, such as LEP or future lepton colliders, or by flavor measurements. The operators in classes 5, 6, and 7 lead to contributions to the DY amplitude that grow with energy and that interfere with SM amplitudes, therefore generating  $s/\Lambda^2$  contributions in the squared amplitude. The effect of these operators in the DY process have been extensively studied in the literature. Finally, operators in classes 3 and 8 lead to contributions to the DY amplitude that grow with energy, but do not interfere with the SM amplitude, generating contributions to the squared amplitude that are proportional to  $v^2 s/\Lambda^4$  (for class 3) and  $s^2/\Lambda^4$  (for class 8), respectively. Considering only the first two generations, which are those relevant for the present paper, we rewrite these operators, as

$$\begin{aligned} \mathcal{L}_{\psi^2 X \bar{\psi}} &= \frac{1}{\Lambda^2} \sum_{p=e,\mu} \left[ (\bar{\ell}_p \sigma^{\mu\nu} e_p) (c_{e_p B} B_{\mu\nu} + c_{e_p W} \tau^I W_{\mu\nu}^I) \varphi + (\bar{q}_p \sigma^{\mu\nu} d_p) (c_{d_p B} B_{\mu\nu} + c_{d_p W} \tau^I W_{\mu\nu}^I) \varphi \right. \\ &\quad \left. + (\bar{q}_p \sigma^{\mu\nu} u_p) (c_{u_p B} B_{\mu\nu} + c_{u_p W} \tau^I W_{\mu\nu}^I) \tilde{\varphi} + \text{h.c.} \right], \\ \mathcal{L}_{\psi^4} &= \frac{1}{\Lambda^2} \sum_{\substack{p=e,\mu \\ r=u,d,s,c}} \left[ c_{\ell_p e_p d_q} (\bar{\ell}_p^j e_p) (\bar{d}_r q_r^j) + c_{\ell_p e_p q u}^{(1)} (\bar{\ell}_p^j e_p) \epsilon_{jk} (\bar{q}_r^k u_r) \right. \\ &\quad \left. + c_{\ell_p e_p q u}^{(3)} (\bar{\ell}_p^j \sigma_{\mu\nu} e_p) \epsilon_{jk} (\bar{q}_r^k \sigma^{\mu\nu} u_r) + \text{h.c.} \right], \end{aligned} \tag{1.2}$$

where we have introduced the dimensionless Wilson coefficients  $c_i$  and we have made explicit our assumption of a diagonal flavor structure in the lepton sector and of flavor universality in the quark sector (the Wilson coefficients of the four-fermion operators do not depend on the quark flavor index  $r$ ). The UV origin of these operators can be diverse and a detailed discussion of explicit models is beyond the phenomenological scope of this paper. However, we present in Appendix F a brief overview of possible UV completions that can generate some of these operators, possibly with a sizable coefficient.

As it will be clear in the following, the main idea of this paper is on the one hand to profit of the energy growth of the chirality-breaking operators discussed above, and on the other hand to isolate their contribution from the SM and the SMEFT operators that interfere with the SM by considering observables where the contribution of the latter is

---

<sup>1</sup>The growth with energy of the four-fermion interactions is entirely determined by the spinor polarization of the external fermions, which carry a power of  $\sqrt{E}$ , and not by the Lorentz structure of the operator, so that scalar, vector, and tensor four-fermion operators all lead to amplitudes that grow with the square of the energy  $s$ .

suppressed. To do so, we focus on the angular distribution of the lepton pair in the DY process, which is sensitive to the chirality structure of the operators, and on the violation of the Lam-Tung relation [15, 16], which guarantees a suppression of the SM contribution, and of the NP contribution with the same chirality structure of the SM, to the relevant observables. On top of considering observables that are suppressed for the SM due to the Lam-Tung relation, we also exploit the growing-with-energy behavior of the chirality-breaking operators to enhance their contribution with respect to the SM.

The paper is organized as follows. In Section 2 we describe the angular decomposition of the Drell-Yan differential cross-section, the related angular coefficients, and the Lam-Tung relation, which is a key ingredient in our analysis. In Section 3 we review the experimental status of the measurements of the angular coefficients in DY, while in Section 4 we present our precise estimates of the cross-section and of the angular observables in the SM, both in the transverse momentum and invariant mass distributions of the lepton pair, for the LHC and HL-LHC. In Section 5 we discuss the Lam-Tung relation and compute the contribution of the chirality-breaking SMEFT operators to the relevant observables. In Section 6 we present our analysis of the LHC and HL-LHC sensitivity on the relevant SMEFT operators, based on a likelihood fit to the aforementioned observables. In Section 7 we summarize the results, while in Section 8 we draw our conclusions. The paper is complemented by a number of appendices reporting our choices on the definition of the observables and some analytic results relevant for our analysis.

## 2 Angular coefficients and the $A_0 - A_2$ observable

The fully-differential inclusive cross-section of the neutral DY process  $pp \rightarrow \ell^+ \ell^-$ , where  $\ell$  is a lepton<sup>2</sup>, can be expressed in terms of the invariant mass  $m_{\ell\ell}$ , the transverse momentum  $p_T^{\ell\ell}$ , the rapidity  $y_{\ell\ell}$  of the lepton pair, and the polar and azimuthal angles  $\theta$  and  $\phi$  of the negative charged lepton in the Collins-Soper (CS) frame [17] (see Appendix A for details), as

$$\begin{aligned} \frac{d\sigma}{dm_{\ell\ell}^2 dp_T^{\ell\ell} dy_{\ell\ell} d\cos\theta d\phi} &= \frac{3}{16\pi} \frac{d\sigma}{dm_{\ell\ell}^2 dp_T^{\ell\ell} dy_{\ell\ell}} \\ &\left\{ (1 + \cos^2\theta) + \frac{1}{2}A_0(1 - 3\cos^2\theta) + A_1 \sin 2\theta \cos\phi \right. \\ &+ \frac{1}{2}A_2 \sin^2\theta \cos 2\phi + A_3 \sin\theta \cos\phi + A_4 \cos\theta \\ &\left. + A_5 \sin^2\theta \sin 2\phi + A_6 \sin 2\theta \sin\phi + A_7 \sin\theta \sin\phi \right\}. \end{aligned} \quad (2.1)$$

The coefficients  $A_l$  are dimensionless and can be extracted from experimental data by making a fit to the angular distribution of the lepton pair. This expression is completely general and also holds in the presence of QCD and electroweak corrections.

A crucial observable for this process is  $A_0 - A_2$ , which, according to the so-called Lam-Tung relation [15], is expected to vanish in the Standard Model (SM) up to corrections of

---

<sup>2</sup>Throughout this paper, we use  $\ell$  to denote either an electron or a muon. Although electrons and muons differ from an experimental point of view, they have been treated equivalently in our theoretical discussion.

order  $\mathcal{O}(\alpha_S)$ . As a result, the SM contribution to this observable is suppressed by QCD effects at order  $\mathcal{O}(\alpha_S^2)$ , making it an excellent probe for potential new physics (NP) effects. Moreover, as noted in Ref. [9], the only dimension-six operators that can violate the Lam-Tung relation are the chirality-breaking ones, specifically those belonging to classes 3 and 8 discussed in the previous section. For these reasons,  $A_0 - A_2$  stands out as a distinctive observable where the contribution of such operators can be effectively isolated. This makes it a particularly suitable candidate for constraining them, especially when compared to the differential cross-section, where their effect is subleading relative to operators that do interfere with the SM. Accordingly, we propose a systematic study of the sensitivity of the LHC and HL-LHC to chirality-breaking SMEFT operators via the  $A_0 - A_2$  observable.

The  $A_l$  coefficients are defined through expectation values of suitable combinations of spherical harmonics in the  $\theta$  and  $\phi$  angles, normalized to the cross-section integrated over such angles.<sup>3</sup> In particular, for each bin of  $m_{\ell\ell}$ ,  $p_{T,\ell\ell}$ , and  $y_{\ell\ell}$ , one can define

$$S_l = \langle P_l(\cos\theta, \phi) \rangle = \frac{\int d\sigma(\cos\theta, \phi, m_{\ell\ell}, p_{T,\ell\ell}^{\ell\ell}, y_{\ell\ell}) d\cos\theta d\phi P_l(\cos\theta, \phi)}{\int d\sigma(\cos\theta, \phi, m_{\ell\ell}, p_{T,\ell\ell}^{\ell\ell}, y_{\ell\ell}) d\cos\theta d\phi}. \quad (2.2)$$

It can be verified that the  $P_l(\cos\theta, \phi)$  choice that projects the amplitude onto the  $A_l$  coefficients is given by

$$\begin{aligned} S_0 &= \langle P_0(\cos\theta, \phi) \rangle = \langle \frac{1}{2} (1 - 3\cos^2\theta) \rangle = \frac{3}{20} \left( A_0 - \frac{2}{3} \right), \\ S_1 &= \langle P_1(\cos\theta, \phi) \rangle = \langle \sin 2\theta \cos \phi \rangle = \frac{1}{5} A_1, \\ S_2 &= \langle P_2(\cos\theta, \phi) \rangle = \langle \sin^2\theta \cos 2\phi \rangle = \frac{1}{10} A_2, \\ S_3 &= \langle P_3(\cos\theta, \phi) \rangle = \langle \sin\theta \cos \phi \rangle = \frac{1}{4} A_3, \\ S_4 &= \langle P_4(\cos\theta, \phi) \rangle = \langle \cos\theta \rangle = \frac{1}{4} A_4, \\ S_5 &= \langle P_5(\cos\theta, \phi) \rangle = \langle \sin^2\theta \sin 2\phi \rangle = \frac{1}{5} A_5, \\ S_6 &= \langle P_6(\cos\theta, \phi) \rangle = \langle \sin 2\theta \sin \phi \rangle = \frac{1}{5} A_6, \\ S_7 &= \langle P_7(\cos\theta, \phi) \rangle = \langle \sin\theta \sin \phi \rangle = \frac{1}{4} A_7, \end{aligned} \quad (2.3)$$

so that the  $A_l$  coefficients can be extracted from the  $S_l$  ones as

$$\begin{aligned} A_0 &= \frac{20}{3} S_0 + \frac{2}{3}, & A_1 &= 5S_1, \\ A_2 &= 10S_2, & A_3 &= 4S_3, \\ A_4 &= 4S_4, & A_5 &= 5S_5, \\ A_6 &= 5S_6, & A_7 &= 4S_7. \end{aligned} \quad (2.4)$$

---

<sup>3</sup>see the latest discussion in Refs. [18–22].



The exact relation between the  $P_l(\cos \theta, \phi)$  functions and the ordinary spherical harmonics is given in Appendix B. The SM contribution to the  $A_l$  observables can be explicitly written as a function of

$$S_l^{\text{SM}} = \frac{\int d\sigma^{\text{SM}}(\cos \theta, \phi, m_{\ell\ell}, p_T^{\ell\ell}, y_{\ell\ell}) d\cos \theta d\phi P_l(\cos \theta, \phi)}{\int d\sigma^{\text{SM}}(\cos \theta, \phi, m_{\ell\ell}, p_T^{\ell\ell}, y_{\ell\ell}) d\cos \theta d\phi}. \quad (2.5)$$

As already mentioned, in this paper we do not make use of the lepton system rapidity  $y_{\ell\ell}$  distribution, and we only consider the dependence of the  $A_0 - A_2$  observables either on the transverse momentum  $p_T^{\ell\ell}$  or on the invariant mass  $m_{\ell\ell}$  distribution of the lepton pair.

When any of the dipole, scalar, or tensor four-fermion operators, corresponding to the Wilson coefficient  $c_{\text{NP}}$  is switched on, we can rewrite the differential cross-section, integrated over  $y_{\ell\ell}$ , as

$$d\sigma(\cos \theta, \phi, m_{\ell\ell}, p_T^{\ell\ell}) = d\sigma^{\text{SM}}(\cos \theta, \phi, m_{\ell\ell}, p_T^{\ell\ell}) + \left(\frac{c_{\text{NP}}}{\Lambda^2}\right)^2 d\tilde{\sigma}^{\text{NP}}(\cos \theta, \phi, m_{\ell\ell}, p_T^{\ell\ell}), \quad (2.6)$$

where  $d\tilde{\sigma}^{\text{NP}}$  is, up to the NP coefficient  $(c_{\text{NP}}/\Lambda^2)^2$ , the differential cross-section generated by the NP operator, which does not interfere with the SM. Substituting Eq. (2.6) into Eq. (2.2), we obtain the  $S_l$  observable in the presence of NP contributions:

$$S_l = \frac{\int d\sigma^{\text{SM}}(\cos \theta, \phi, m_{\ell\ell}, p_T^{\ell\ell}) d\cos \theta d\phi P_l(\cos \theta, \phi)}{d\sigma^{\text{SM}}(m_{\ell\ell}, p_T^{\ell\ell}) + \left(\frac{c_{\text{NP}}}{\Lambda^2}\right)^2 d\tilde{\sigma}^{\text{NP}}(m_{\ell\ell}, p_T^{\ell\ell})} + \left(\frac{c_{\text{NP}}}{\Lambda^2}\right)^2 \frac{\int d\tilde{\sigma}^{\text{NP}}(\cos \theta, \phi, m_{\ell\ell}, p_T^{\ell\ell}) d\cos \theta d\phi P_l(\cos \theta, \phi)}{d\sigma^{\text{SM}}(m_{\ell\ell}, p_T^{\ell\ell}) + \left(\frac{c_{\text{NP}}}{\Lambda^2}\right)^2 d\tilde{\sigma}^{\text{NP}}(m_{\ell\ell}, p_T^{\ell\ell})}, \quad (2.7)$$

where we made explicit the integration of the denominator over  $\cos \theta$  and  $\phi$  by omitting the corresponding variables in the argument of the differential cross-sections. The  $A_l$  observables in the presence of NP contributions can then be obtained from Eq. (2.7) by using Eq. (2.4).

In the limit  $(c_{\text{NP}}/\Lambda^2) \rightarrow 0$ , this expression reduces to the SM one in Eq. (2.5). Moreover, we know that, in this limit,  $A_0 - A_2$  is non-zero only starting from  $\mathcal{O}(\alpha_S^2)$ , due to the Lam-Tung relation. This means that, to correctly account for the SM contribution to the  $A_0 - A_2$  observable, we need to evaluate the SM differential cross-section at order  $\mathcal{O}(\alpha_S^2)$ . Equation (2.7) also shows that generally, even though the SM and the SMEFT contributions do not interfere, their contributions to the  $S_l$  observables, and therefore also to the  $A_l$  and  $A_0 - A_2$  combinations, can not be simply disentangled, since the denominator contains both the SM and the NP contributions. In other words, the behavior with respect to the Wilson coefficients  $c_{\text{NP}}$  of the  $A_l$  observables can be approximated as quadratic only in the limit where the NP contribution to the differential cross-section is subdomi-

nant with respect to the SM one. This may not be the case in the regions of the phase space where the SMEFT contribution is enhanced, for example at large invariant mass or transverse momentum of the lepton pair, which turn out to be the most sensitive regions to constrain the chirality-breaking operators. Therefore, in our analysis we present results obtained both with the exact relation of Eq. (2.7), which would of course be subject to corrections from operators of dimension higher than six that we do not consider, and with its quadratic approximation in  $c_{\text{NP}}/\Lambda^2$ , which corresponds to a fixed order truncation in the SMEFT expansion. This allows one to assess the possible impact of higher-order terms in the SMEFT expansion on the bounds that we derive.

In order to compute the  $p_T^{\ell\ell}$  and  $m_{\ell\ell}$  dependence of the  $A_l$  observables we proceeded as follows. We estimated the SM differential cross-section for the process  $pp \rightarrow \ell^+\ell^-$  at  $\mathcal{O}(\alpha_S^2)$  by generating events with the `MinNLOPS` [23, 24] Monte Carlo generator, implemented in the `POWHEG` framework [25–27]. We have checked that the inclusion of showering effects, available in the `MinNLOPS` framework through a matching with `PYTHIA8` [28–30] showering, does not affect the results of our analysis, and we therefore proceeded computing parton level events with a lepton–anti-lepton pair and up to two jets in the final state. Notice that, since we consider the differential  $p_T^{\ell\ell}$  distribution for a finite  $p_T^{\ell\ell} \geq 10$  GeV cut, we could have in principle computed the NLO QCD correction to the process  $pp \rightarrow \ell^+\ell^- + j$ . However, we decided to use the `MinNLOPS` framework which allowed us to directly generate weighted events in Les Houches (lhe) format [31] and to properly check the effect of the parton showering.

The generated SM events were used to define the differential SM cross-sections  $d\sigma^{\text{SM}}/dp_T^{\ell\ell}$  within a window  $80 \text{ GeV} < m_{\ell\ell} < 100 \text{ GeV}$  and  $d\sigma^{\text{SM}}/dm_{\ell\ell}^2$  in the region  $p_T^{\ell\ell} > 10 \text{ GeV}$ , by binning the events in the relevant kinematic variable.

In order for the differential cross-section to be defined at finite  $p_T^{\ell\ell}$ , the SMEFT contribution was computed analytically by considering the process  $pp \rightarrow \ell^+\ell^- + j$  at the leading order in QCD. The partonic cross-sections for all sub-processes have been calculated using the `FeynCalc` [32] and `FeynArts` [33] packages in `Mathematica` [34], after truncating the squared amplitude at  $\mathcal{O}(1/\Lambda^4)$ , which is equivalent to considering a single NP insertion. The hadronic cross-section was then derived by convoluting these results with the PDFs. For this purpose, we employed the `ManeParse` package [35] for `Mathematica`, which provides all the necessary tools for PDF integration. We adopted the PDF set `NNPDF31_nnlo_as_0118` (ID 303600 in the LHAPDF [36] set), neglecting contributions from the  $b$  and  $t$  quarks. Details about the analytical expression of the integral can be found in appendix C. This procedure allowed us to compute the differential cross-sections  $d\tilde{\sigma}^{\text{NP}}/dp_T^{\ell\ell}$  and  $d\tilde{\sigma}^{\text{NP}}/dm_{\ell\ell}^2$  in the same kinematic region as the SM ones, and to use them in Eq. (2.7) to compute the  $S_l$  and  $A_l$  observables in the presence of NP contributions. The evaluation of Eq. (2.7) also required the calculation of the projections of the cross-section onto the corresponding angular polynomials  $P_l(\cos\theta, \phi)$ . This was done by Monte Carlo integration for the SM, using the generated events, and by numerical integration of the analytic expression for the NP contributions.

## 2.1 Monte Carlo simulation and uncertainty estimation

The angular observables defined in the previous section can be predicted theoretically by Monte Carlo estimation of the integrals. Given a sample of weighted events  $i$  in bin  $I$  with weights  $w_i$ , the cross-section in that bin is given by

$$\sigma_I = \sum_{i \in I} w_i. \quad (2.8)$$

The angular observables in bin  $I$  are then defined from the projections of the cross-section in that bin on the corresponding polynomial functions  $P_l(\cos\theta, \phi)$ , which appear in the numerator of Eq. (2.2). We can compute this by multiplying the MC weights  $w_i$  by the value of the relevant polynomial functions  $P_l^i(\cos\theta, \phi)$ , given in Eq. (2.4), computed for the  $i$ -th event kinematic, and by defining a new set of angular weights

$$w_i^{(l)} = w_i P_l^i(\cos\theta, \phi). \quad (2.9)$$

Then, the differential cross-section projected over the polynomial functions  $P_l(\cos\theta, \phi)$ , that we simply denote by  $\sigma_I^{(l)}$ , is given by

$$\sigma_I^{(l)} = \sum_{i \in I} w_i^{(l)}. \quad (2.10)$$

This projection can be used to estimate the value of the  $S_{l,I}$  observables of Eq. (2.3) in each bin  $I$

$$S_{l,I} = \frac{\sigma_I^{(l)}}{\sigma_I} \quad (2.11)$$

and, in turn, to compute the  $A_{l,I}$  observables through Eq. (2.4).

Extracting a meaningful bound on the new physics contribution from the differential angular observables  $A_l$ , and in particular from the  $A_0 - A_2$  combination, requires a careful estimate of the expected experimentally measured values and uncertainties of the observables, especially for what concerns the SM contribution. Given the very large statistics available at the LHC for the DY process, at relatively low  $p_T^{\ell\ell}$  and for di-lepton invariant masses  $m_{\ell\ell}$  not far above the  $Z$  boson mass, the uncertainty is dominated by experimental systematics. Since no recent analysis of the multi-differential DY cross-section is available, and based on the existing experimental results, we decided to make the simplifying assumption of a flat, uncorrelated, 3% uncertainty on the differential cross-section in all bins.

Concerning the statistical uncertainty, which becomes dominant in corner regions of the phase space, such as very large  $p_T^{\ell\ell}$  and/or  $m_{\ell\ell}$  much above the  $Z$  boson mass, we generated enough statistics to cover the expected experimental statistics at the LHC with  $\mathcal{L} = 300 \text{ fb}^{-1}$ ,<sup>4</sup> which is the target integrated luminosity of the LHC and extrapolated with

---

<sup>4</sup>This required the generation of about a billion events for the  $p_T^{\ell\ell}$  distribution, which is at the edge of what we could afford with our computing resources. The number of events generated for the  $m_{\ell\ell}$  distribution was substantially lower, thanks to the ability of the `MINNLOps` generator to cut on the di-lepton invariant

a factor of square root of ten to the HL-LHC with  $\mathcal{L} = 3 \text{ ab}^{-1}$ . The central values were kept unchanged in this extrapolation.

In order to estimate the central values and the statistical uncertainties in each bin of the two distributions, we have proceeded as follows. We denoted with  $n_I^{\text{MC}}$  the available number of MC-generated events in each bin  $I$  and with

$$\sigma_I^{\text{MC}} = \sum_{i \in I} w_i \quad (2.12)$$

the MC-estimated cross-section in that bin. We then fixed an initial value for the number of events corresponding to the experimental observation with a given integrated luminosity  $\mathcal{L}$

$$n_I^{\text{exp}} = \sigma_I^{\text{MC}} \times \mathcal{L}. \quad (2.13)$$

To estimate the expected value and the standard deviation of the differential cross-section and of the angular observables in each bin (of the relevant kinematic distribution), we simulated pseudo-experiments, each corresponding to the statistics expected at the LHC with  $\mathcal{L} = 300 \text{ fb}^{-1}$ .<sup>5</sup> Pseudo experiments were drawn from the available MC sample with replacement.<sup>6</sup> In order to fix the correct value of the cross-section, for each pseudo-experiment we rescaled the value of the corresponding weights. In order to also introduce a fluctuation in the normalization, and not only in the shape, we also considered fluctuations in the normalization, computed from the original MC sample. Obviously, fluctuations on the normalization only affect the cross-section estimate and not the angular coefficients, which are built from ratios. The detailed procedure is outlined in the following:

- For each pseudo-experiment  $p$  and bin  $I$ , we consider a Poisson fluctuation of the number of MC events

$$n_I^{\text{MC},(p)} = \text{Poisson}(\mu = n_I^{\text{MC}}), \quad (2.14)$$

and draw, with replacement,  $n_I^{\text{MC},(p)}$  events from the available MC events. We use this sample to estimate a fluctuation of the cross-section in that bin, that we denote by  $\sigma_I^{\text{MC},(p)}$ , and that we use as fluctuating normalization of the cross-section in that bin.

- For each pseudo-experiment  $p$  and bin  $I$ , we consider a Poisson fluctuation of the number of experimental events

$$n_I^{\text{exp},(p)} = \text{Poisson}(\mu = n_I^{\text{exp}}), \quad (2.15)$$

and draw, with replacement,  $n_I^{\text{exp},(p)}$  from the available MC events.

---

mass.

<sup>5</sup>The result for  $\mathcal{L} = 3 \text{ ab}^{-1}$  has been obtained assuming that the variance scales with the ration of the number of events and therefore scaling the error with a square root of ten.

<sup>6</sup>When the available MC sample is smaller or roughly equal in size than the expected statistics, such as in low  $p_T^{\ell\ell}$  bins, our procedure may underestimate the standard deviation. On the other hand these are the bins where the expected statistical uncertainty is much smaller than the expected systematic uncertainty, so that the effect of such underestimation becomes negligible.

- For each pseudo-experiment  $p$  and bin  $I$ , we use the corresponding  $n_I^{\text{exp},(p)}$  events to define a new set of normalized weights

$$w_i^{\text{exp},(p)} = \kappa_I^{(p)} w_i^{(p)} \quad \forall i \in I, \quad (2.16)$$

with normalization

$$\kappa_I^{(p)} = \frac{\sigma_I^{\text{MC},(p)}}{\sum_{i \in I} w_i^{(p)}}. \quad (2.17)$$

Notice that this definition does automatically set the corresponding cross-section to its correct fluctuating normalization:

$$\sigma_I^{\text{exp},(p)} \equiv \sum_{i \in I} w_i^{\text{exp},(p)} = \kappa_I^{(p)} \sum_{i \in I} w_i^{(p)} = \sigma_I^{\text{MC},(p)}. \quad (2.18)$$

- For each pseudo-experiment  $p$  and bin  $I$ , we use the corresponding  $n_I^{\text{exp},(p)}$  events to define a new set of normalized angular weights, analog to those in Eq. (2.9),

$$w_i^{\text{exp},(l),(p)} = \kappa_I^{(p)} w_i^{(p)} P_l^{i,(p)}(\cos \theta, \phi) \quad \forall i \in I. \quad (2.19)$$

- For each pseudo-experiment  $p$  and bin  $I$ , we use the new set of normalized angular weights to estimate the cross-section angular projections as

$$\sigma_I^{\text{exp},(l),(p)} = \sum_{i \in I} w_i^{\text{exp},(l),(p)} = \kappa_I^{(p)} \sum_{i \in I} w_i^{(p)} P_l^{i,(p)}(\cos \theta, \phi). \quad (2.20)$$

- For each pseudo-experiment  $p$  and bin  $I$ , we use Eqs. (2.18) and (2.19) to compute the  $S_l$ 's observables as

$$S_{l,I}^{\text{exp},(p)} = \frac{\sigma_I^{\text{exp},(l),(p)}}{\sigma_I^{\text{exp},(p)}} = \frac{\sum_{i \in I} w_i^{(p)} P_l^{i,(p)}(\cos \theta, \phi)}{\sum_{i \in I} w_i^{(p)}}, \quad (2.21)$$

which is, as expected, independent on the cross-section normalization  $\kappa_I^{(p)}$ .

- We estimate the central values and (one dimensiona) covariance matrix of the differential cross-section as

$$\mu_{\sigma_I} = \text{Mean}_{p \in \mathcal{P}} \left( \sigma_I^{\text{MC},(p)} \right), \quad (\Sigma_{\sigma_I, \sigma_I})^{\text{stat}} = \text{Var}_{p \in \mathcal{P}} \left( \sigma_I^{\text{MC},(p)} \right), \quad (2.22)$$

where we denoted with  $\text{Mean}_{p \in \mathcal{P}}$  and  $\text{Var}_{p \in \mathcal{P}}$  the mean and variance computed over a set of 100 pseudo-experiments.

- We estimate the central values and covariance matrix of the  $S_l$ 's observables as

$$\mu_{S_{l,I}} = \text{Mean}_{p \in \mathcal{P}} \left( S_{l,I}^{\text{exp},(p)} \right), \quad (\Sigma_{S_{l,I}, S_{m,I}})^{\text{stat}} = \text{Cov}_{p \in \mathcal{P}} \left( S_{l,I}^{\text{exp},(p)}, S_{m,I}^{\text{exp},(p)} \right), \quad (2.23)$$

Collab.	Year	Energy	Luminosity	Observable	Ref.
ATLAS	2024	5.02, 13 TeV	255, 338 pb <sup>-1</sup>	$d\sigma_{\ell\ell}/dp_{T,u}$	[37] ⓘ
ATLAS	2024	8 TeV	20.2 fb <sup>-1</sup>	$d\sigma_{\ell\ell}/dp_{T,u}dy_{\ell\ell}$	[38] ⓘ
CMS	2023	13 TeV	36.3 fb <sup>-1</sup>	$d\sigma_{\ell\ell}/dp_{T,u}dm_{\ell\ell}^2, d\sigma_{\ell\ell}/d\phi_{\eta}^*dm_{\ell\ell}^2$	[39] ⓘ
LHCb	2022	13 TeV	5.1 fb <sup>-1</sup>	$A_0, \dots, A_7$ as functions of $p_{T,u}$	[40] ⓘ
ATLAS	2020	13 TeV	36.1 fb <sup>-1</sup>	$d\sigma_{\ell\ell}/dp_{T,u}, d\sigma_{\ell\ell}/d\phi_{\eta}^*$	[41] ⓘ
CMS	2019	13 TeV	35.9 fb <sup>-1</sup>	$d\sigma_{\ell\ell}/dp_{T,u}, d\sigma_{\ell\ell}/d y_{\ell\ell} , d\sigma_{\ell\ell}/d\phi_{\eta}^*$	[42] ⓘ
CMS	2019	13 TeV	2.8 <sup>(μ)</sup> /2.3 <sup>(e)</sup> fb <sup>-1</sup>	$d\sigma_{\ell\ell}/dm_{\ell\ell}^2$	[43] ⓘ
CMS	2018	8 TeV	19.7 fb <sup>-1</sup>	$d\sigma_{\ell\ell}/d\phi_{\eta}^*, d\sigma_{\ell\ell}/d\phi_{\eta}^*d y_{\ell\ell} $	[44] ⓘ
ATLAS	2017	8 TeV	20.2 fb <sup>-1</sup>	$d\sigma_{\ell\ell}/dm_{\ell\ell}^2d y_{\ell\ell} d\cos\theta^*$	[45] ⓘ
CMS	2017	8 TeV	18.4 fb <sup>-1</sup>	$d\sigma_{\ell\ell}/dp_{T,u}$	[46] ⓘ
ATLAS	2016	8 TeV	20.3 fb <sup>-1</sup>	$d\sigma_{\ell\ell}/dm_{\ell\ell}^2d y_{\ell\ell} , d\sigma_{\ell\ell}/dm_{\ell\ell}^2d \Delta\eta_{\ell\ell} $	[47] ⓘ
ATLAS	2016	8 TeV	20.3 fb <sup>-1</sup>	$A_0, \dots, A_7$ as functions of $p_{T,u}$	[48] ⓘ
ATLAS	2016	8 TeV	20.3 fb <sup>-1</sup>	$d\sigma_{\ell\ell}/dp_{T,u}, d\sigma_{\ell\ell}/d\phi_{\eta}^*$	[49] ⓘ
CMS	2015	8 TeV	19.7 fb <sup>-1</sup>	$A_0, \dots, A_7$ as functions of $p_{T,u}$	[50] ⓘ
CMS	2015	8 TeV	19.7 fb <sup>-1</sup>	$d\sigma_{\ell\ell}/dp_{T,u}, d\sigma_{\ell\ell}/d y_{\ell\ell} $	[51] ⓘ

**Table 2:** Summary of the possibly relevant experimental measurements of Drell-Yan observable over the last ten years. For ease of reading, hovering over the info icon shows the bibliography item.

where we denoted with  $\text{Mean}_{p \in \mathcal{P}}$  and  $\text{Cov}_{p \in \mathcal{P}}$  the mean and covariance matrix computed over a set of 100 pseudo-experiments.

- Analogously, we estimate the central values and covariance matrix of the  $A_l$  observables through Eq. (2.4).

Once the central values  $\mu_{\mathcal{O}}$  and covariance matrix  $(\Sigma_{\mathcal{O},\mathcal{O}'}^{\text{stat}})^{\text{stat}}$  of the observables  $\mathcal{O}$  are computed, we combine the uncertainties with the corresponding quantities parametrizing the systematic uncertainty  $(\Sigma_{\mathcal{O},\mathcal{O}'}^{\text{syst}})^{\text{syst}}$  and get the final estimate of the observables as

$$\mu_{\mathcal{O}} \pm \sqrt{\Sigma_{\mathcal{O},\mathcal{O}}} \quad \text{with} \quad \Sigma_{\mathcal{O},\mathcal{O}'} = \Sigma_{\mathcal{O},\mathcal{O}'}^{\text{stat}} + \Sigma_{\mathcal{O},\mathcal{O}'}^{\text{syst}}. \quad (2.24)$$

### 3 Experimental status

The measurements relevant for the present paper fall in the realm of precision measurements for new physics searches.<sup>7</sup> Such precision measurements usually take a long term experimental effort and this is why not many such measurements are already available from LHC Run 2 and Run 3. Here we briefly summarize the most relevant existing measurements in the Drell-Yan channel, and use the information we can gather from them to motivate our assumptions on the uncertainties discussed in the previous section. Table 2 lists the measurements of differential cross-sections and angular coefficients in di-lepton final states performed over the past decade.

As it can immediately be seen from the table, only a single measurement of the angular coefficients from each experiment ATLAS, CMS, and LHCb is available. The first two measurements are at 8 TeV and an integrated luminosity of around 20 fb<sup>-1</sup>, while the LHCb

<sup>7</sup>We omitted LHCb measurements of the inclusive cross-section since they generally have less statistics. Obviously, in the case in which the forward region becomes more relevant the LHCb measurements become important.

measurement in the forward region is the only measurement of the angular coefficient to date at an energy of 13 TeV, with an integrated luminosity of  $5.1 \text{ fb}^{-1}$ . No updated measurements of the angular coefficients have yet been performed at 13 TeV, where the LHC has collected a much larger integrated luminosity. The measurements of the differential cross-section are more abundant, with different differential distributions measured at different energies and integrated luminosities. However, even the most recent measurements at 13 TeV are performed with a limited integrated luminosity of approximately  $36 \text{ fb}^{-1}$ , which is only a small fraction of the total integrated luminosity collected at 13 TeV during Run 2 (around  $160 \text{ fb}^{-1}$ ).

Both the CMS [50] and ATLAS [48] measurements of the angular coefficients at 8 TeV are performed in the  $Z$ -boson mass peak region, and, to take into account the effect of the finite acceptance on the leptons, which affects the angular distributions in Eq. (2.1), are performed through matching with Monte Carlo templates of the different angular observables in the  $\theta$ - $\phi$  plane. Entering in the details of the experimental measurements is beyond the scope of this paper, and we refer the reader to the original experimental papers for more details. Here, we are only interested in understanding the expectation about the measurement uncertainties, which we need to consider for a realistic projection of the sensitivity to new physics in the angular coefficients.

From Tables 11 to 14 of Ref. [48], we can see that the statistical and systematic uncertainties on the  $p_T^{\ell\ell}$  distribution of the  $A_0$ ,  $A_2$ , and  $A_0 - A_2$  observables are comparable over the whole spectrum, but in the last few bins, where, obviously, the statistical uncertainty dominates. Even though most of the systematic uncertainties, such as Monte Carlo statistics, have large margins for improvement, it is reasonable to expect that, with the full LHC and HL-LHC integrated luminosity, the systematic uncertainties will be dominant in the whole spectrum, but the last few bins, where the statistical uncertainty will still be dominant. We have already discussed in the previous section how we model the statistical uncertainty through pseudo-experiments simulation. Concerning the systematic uncertainty, assuming a projected uncertainty directly on the  $A_l$  coefficients from the aforementioned angular analyses is not possible, since we can not guess how this will improve in the future. However, we can take the expected systematic uncertainties on the differential cross-section measurements from recent 13 TeV analyses as a guideline. We consider in particular the ATLAS analysis of Ref. [41] as reference analysis of the  $p_T^{\ell\ell}$  spectrum and the CMS analysis of Ref. [43] as reference analysis of the  $m_{\ell\ell}$  spectrum. We adopt the same binning for the two distributions and use the experience of those analyses to motivate our assumption on the systematic uncertainties on the differential cross-sections. Starting from such uncertainties, and assuming the same uncertainties for the cross-sections projections on the different angular polynomials, we propagate the uncertainty to the  $A_l$  coefficients. The result is consistent with a systematic uncertainty that dominates in the low  $p_T^{\ell\ell}$  and  $m_{\ell\ell}$  region (above the  $Z$  boson mass) and becomes subleading in the tails of the distributions.

In the next section, we show projections for the expected measurements of the  $p_T^{\ell\ell}$  and  $m_{\ell\ell}$  distributions, as well as the angular coefficients.



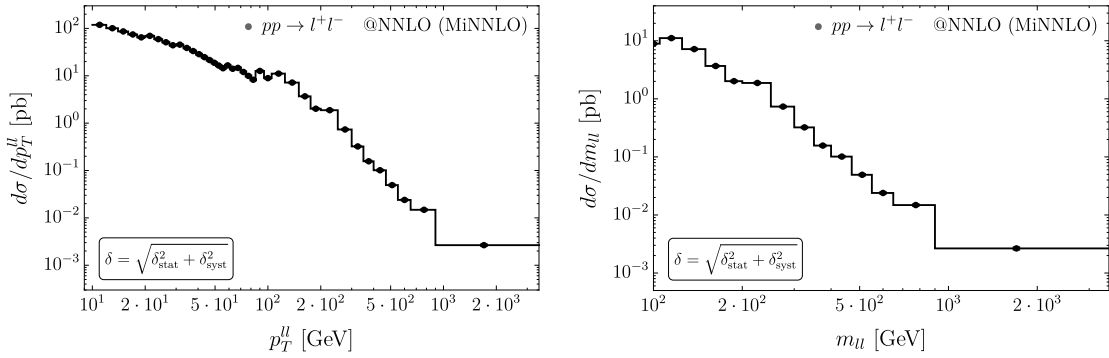


**Figure 1:** Standard Model prediction for the  $p_T^{\ell\ell}$  (left panel) and  $m_{\ell\ell}$  (right panel) spectra in the DY process at the LHC at 13 TeV with 300 fb<sup>-1</sup>. Uncertainties are too small to be visible, so the result is visually the same for both 300 fb<sup>-1</sup> and 3 ab<sup>-1</sup> of integrated luminosity. The exact numerical values (both central values and uncertainties) corresponding to 300 fb<sup>-1</sup> and 3 ab<sup>-1</sup> of integrated luminosity are given in Tables 8 and 12 of Appendix E.

## 4 Standard Model predictions

In this section, we present SM predictions for the  $p_T^{\ell\ell}$  and  $m_{\ell\ell}$  distributions of the cross-section and angular observables in the Drell-Yan process. Such predictions will be combined with predictions of the effect of new physics and used to derive projected limits on the chirality-breaking operator of Eq. (1.2) in the next section.

### 4.1 Transverse momentum distribution

The left panel of Figure 1 shows the SM prediction for the di-lepton  $p_T^{\ell\ell}$  spectrum in the DY process at the LHC at 13 TeV, assuming a flat, uncorrelated systematic uncertainty of 3%, corresponding, for instance, to a 2% systematic from the integrated luminosity measurement and about 2% additional systematic uncertainty, including missing higher orders (scale variation), PDFs, Monte Carlo, and experimental uncertainties. These numbers for the systematic uncertainties are consistent with those reported in the aforementioned ATLAS analysis of Ref. [41], at least for the low and intermediate  $p_T^{\ell\ell}$  region. The high  $p_T^{\ell\ell}$  region has much larger systematic uncertainties, which are clearly statistically dominated. We do not have a clear prescription to project this uncertainty to the future measurements, and therefore we assume the flat 3% uncertainty also for the high  $p_T^{\ell\ell}$  region. Statistical and systematic uncertainties are added in quadrature, and the statistical uncertainty is derived through pseudo-experiments as explained in the previous section. Uncertainties are too small to be visible in the plot, so the result is visually the same for both 300 fb<sup>-1</sup> and 3 ab<sup>-1</sup> of integrated luminosity. The exact numerical values (both central values and uncertainties) corresponding to 300 fb<sup>-1</sup> and 3 ab<sup>-1</sup> of integrated luminosity are given in Table 8 of Appendix E.

Figure 2 shows the SM prediction for the angular coefficients  $A_0$ ,  $A_2$ , and  $A_0 - A_2$  as functions of  $p_T^{\ell\ell}$  in the DY process at the LHC at 13 TeV with two assumptions for the statistical uncertainty: the larger error bars represent the combined statistical and systematic uncertainty with 300 fb<sup>-1</sup> of integrated luminosity, while the smaller error bars



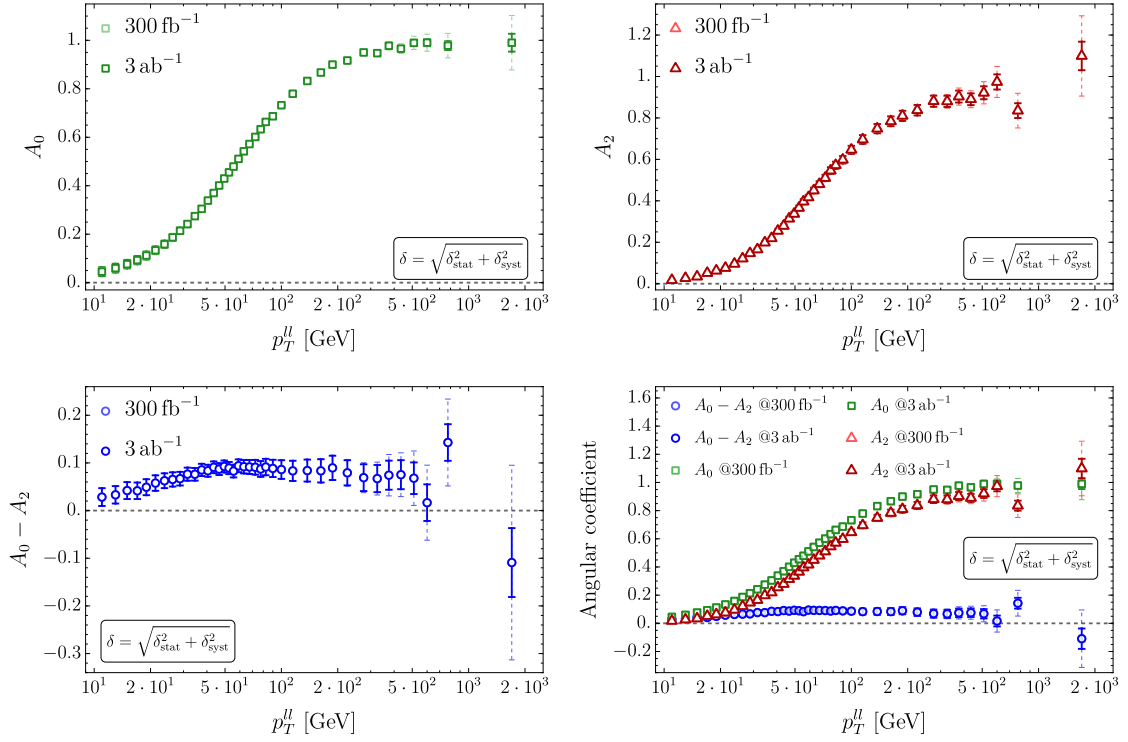


**Figure 2:** Standard Model prediction for the  $p_T^{\ell\ell}$  dependence of the angular observables  $A_0$  (upper left),  $A_2$  (upper right), and  $A_0 - A_2$  (lower left) in the DY process at the LHC at 13 TeV with 300 fb<sup>-1</sup> and 3 ab<sup>-1</sup> both inclusive in rapidity. The lower right panel gives a combined view of the result. The numerical values of the observables appearing in the plots are given in Tables 9, 10, and 11 of Appendix E.

represent the combined statistical and systematic uncertainty with 3 ab<sup>-1</sup> of integrated luminosity. In both cases, we assume a flat, uncorrelated systematic uncertainty of 3% on the measurement of the cross-section and of its angular projections (denoted as  $\sigma_I^{(l)}$  in Section 2) and propagate it to the angular coefficients as explained in the previous section. As before, statistical and systematic uncertainties are added in quadrature, and the statistical uncertainty is derived through pseudo-experiments as explained in the previous section.

Notice that the systematic uncertainty on the  $A_0$  observable is much smaller than that on the  $A_2$  observable, so that, even including correlation among them, the combined systematic uncertainty on  $A_0 - A_2$  is not largely affected, and remains dominated by the uncertainty on  $A_2$ . For this reason we only show the result under the assumption of no correlation among the systematic uncertainties of the different angular coefficients.

All the numbers of the cross-sections and angular coefficients predictions shown in Figures 1 (left) and 2 are summarized in Tables 8, 9, 10, and 11 of Appendix E.

#### 4.2 Invariant mass distribution

The right panel of Figure 1 shows the SM prediction for the di-lepton  $m_{\ell\ell}$  spectrum in the DY process at the LHC at 13 TeV, assuming, as in the case of the  $p_T^{\ell\ell}$  distribution, a flat,

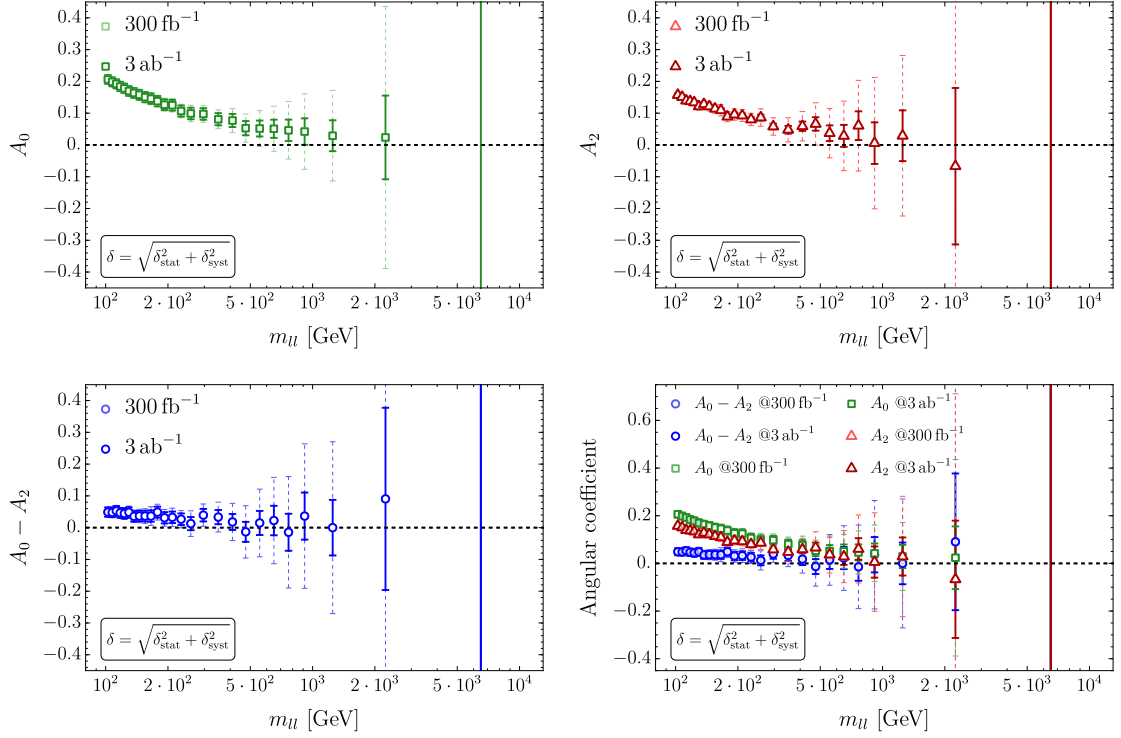


**Figure 3:** Standard Model prediction for the  $m_{\ell\ell}$  dependence of the angular observables  $A_0$  (upper left),  $A_2$  (upper right), and  $A_0 - A_2$  (lower left) in the DY process at the LHC at 13 TeV with  $300 \text{ fb}^{-1}$  and  $3 \text{ ab}^{-1}$  both inclusive in rapidity. The lower right panel gives a combined view of the result. The numerical values of the observables appearing in the plots are given in Tables 13, 14, and 15 of Appendix E.

uncorrelated systematic uncertainty of 3% (see above). These numbers for the systematic uncertainties are consistent with those reported in the aforementioned CMS analysis of Ref. [43], at least for systematic uncertainties that are not statistically dominated. In the high  $m_{\ell\ell}$  region, we do not have a clear procedure to project the systematic uncertainty to the future measurements, and therefore we assume the flat 3% uncertainty also in that region. As before, statistical and systematic uncertainties are added in quadrature, the statistical uncertainty is derived through pseudo-experiments as explained in the previous section, and uncertainties are too small to be visible in the plot, so the result is visually the same for both  $300 \text{ fb}^{-1}$  and  $3 \text{ ab}^{-1}$  of integrated luminosity. The exact numerical values (both central values and uncertainties) corresponding to  $300 \text{ fb}^{-1}$  and  $3 \text{ ab}^{-1}$  of integrated luminosity are given in Table 12 of Appendix E.

Figure 3 shows the SM prediction for the angular coefficients  $A_0$ ,  $A_2$ , and  $A_0 - A_2$  as functions of  $m_{\ell\ell}$  in the DY process at the LHC at 13 TeV with two assumptions for the statistical uncertainty: the larger error bars represent the combined statistical and systematic uncertainty with  $300 \text{ fb}^{-1}$ , while the smaller error bars represent the combined statistical and systematic uncertainty with  $3 \text{ ab}^{-1}$ . In both cases, we assume a flat, uncorrelated systematic uncertainty of 3% on the measurement of the cross-section and of its angular projections (denotes as  $\sigma_I^{(l)}$  in Section 2) and propagate it to the angular coefficients as

explained in the previous section. As before, statistical and systematic uncertainties are added in quadrature, and the statistical uncertainty is derived through pseudo-experiments as explained in the previous section.

Notice that, also in this case, the systematic uncertainty on the  $A_0$  observable is much smaller than that on the  $A_2$  observable, so that, even including correlation among them, the combined systematic uncertainty on  $A_0 - A_2$  is not largely affected, and remains dominated by the uncertainty on  $A_2$ . For this reason we only show the result under the assumption of no correlation among the systematic uncertainties of the different angular coefficients.

All the numbers of the cross-sections and angular coefficients projections shown in Figures 1 (right) and 3 are summarized in Tables 12, 13, 14, and 15 of Appendix E.

## 5 SMEFT predictions

In this section we analyze the effects of the dimension-6 operators introduced in Section 1 on the  $A_0 - A_2$  observable. In particular, we argue that the dipoles and scalar/tensor four-fermion operators are the only dimension-6 operators that can break the Lam-Tung relation at order  $\mathcal{O}(\alpha_S^0)$ , that is when QCD corrections are ignored. This remains true also at order  $\mathcal{O}(\alpha_S)$ , motivating our focus on just these two classes of operators. From now on, we omit the flavor index in the Wilson coefficients, and it is understood that all predictions and constraints hold separately, and identically, for electron and muons.

### 5.1 Lam-Tung relation breaking at $\mathcal{O}(\alpha_S^0)$

At the zero-th order in  $\alpha_S$ , and under the assumption of negligible intrinsic transverse momentum of the partons and of negligible effects from the possible QED radiation, the transverse momentum of the lepton pair vanishes. As a consequence, in the di-lepton rest frame the parton beams are collinear, and, in turn, the  $\hat{z}$  axis of the CS frame (see Appendix A for its definition) lies in the direction of the beams and can be identified with the beam axis, denoted by  $z$ . Therefore, the process features azimuthal symmetry, the CS frame can be identified with the center of mass frame (the  $\phi$  angle is arbitrary), and the angular distribution of the leptons in such frame only depends on the angle  $\theta$ , that is the angle between the negatively charged lepton and the  $z$  axis.

The fully differential cross-section of  $pp \rightarrow \ell^+ \ell^- + X$  in the CS frame in the SM is given by Eq. (2.1). This five-differential cross-section reduces, at the zero-th order in  $\alpha_S$ , to the triple differential cross-section for the process  $pp \rightarrow \ell^+ \ell^-$ . Integrating over the arbitrary angle  $\phi$  we can write

$$\int_0^{2\pi} d\phi \lim_{\alpha_S \rightarrow 0} \left( \frac{d\sigma}{dm_{\ell\ell}^2 dp_T^{\ell\ell} dy_{\ell\ell} d\cos\theta d\phi} \right) = \left( \frac{d\sigma}{dm_{\ell\ell}^2 dy_{\ell\ell} d\cos\theta} \right)_{\text{LO}}. \quad (5.1)$$

Since, at  $\mathcal{O}(\alpha_S^0)$ , Eq. (2.1) only depends on  $\theta$  and not on  $\phi$ , that means that it should hold for arbitrary values of  $\phi$ , then all the terms proportional to functions of  $\phi$  must vanish, implying that only the coefficients  $A_0$  and  $A_4$  can be non-zero in this limit. Therefore, we

	SM	$\mathcal{O}_{(3)}$	$\mathcal{O}_{(1,2,4)}$	$\mathcal{O}_{(5,6,7)}$	$\mathcal{O}_{(8)}$
SM	$(1 \pm \cos \theta)^2$				
$\mathcal{O}_{(3)}$	0	$1 - \cos^2 \theta$			
$\mathcal{O}_{(1,2,4)}$	$(1 \pm \cos \theta)^2$	0	$(1 \pm \cos \theta)^2$		
$\mathcal{O}_{(5,6,7)}$	$(1 \pm \cos \theta)^2$	0	0	$(1 \pm \cos \theta)^2$	
$\mathcal{O}_{(8)}$	0	0	0	0	1

**Table 3:** Dependence on the  $\cos \theta$  angular variable of the squared amplitude of the process  $pp \rightarrow \ell^+ \ell^-$  (at leading order in  $\alpha_S$ ) arising from the interference of the SM and the SMEFT operators considered in our analysis. The notation  $(1 \pm \cos \theta)^2$  is used to indicate that the angular dependence is a linear combination of both  $(1 + \cos \theta)^2$  and  $(1 - \cos \theta)^2$  terms. The operators are labeled as in Section 1:  $\mathcal{O}_{(1,2)}$  are the operators  $\phi^4 D^2$  and  $\psi^2 \phi^3$ ,  $\mathcal{O}_{(3)}$  are the dipole operator  $\psi^2 X \varphi$ ,  $\mathcal{O}_{(4)}$  are the operators  $\psi^2 \varphi^2 D$ ,  $\mathcal{O}_{(5,6,7)}$  are the current-current four-fermion operators, and  $\mathcal{O}_{(8)}$  are the scalar/tensor four-fermion operators. The table is symmetric and we only filled the lower part. The two shaded entries highlight the cases where the Lam-Tung relation is violated.

can formally write the limit in Eq. (5.1) as<sup>8</sup>

$$\int_0^{2\pi} d\phi \lim_{\alpha_S \rightarrow 0} \left( \frac{d\sigma}{dm_{\ell\ell}^2 dp_T^{\ell\ell} dy_{\ell\ell} d\cos\theta d\phi} \right) = \frac{3}{8} \left( \frac{d\sigma}{dm_{\ell\ell}^2 dy_{\ell\ell}} \right)_{\text{LO}} [(1 + \cos^2 \theta) + \frac{1}{2} A_0 (1 - 3 \cos^2 \theta) + A_4 \cos \theta]. \quad (5.2)$$

It is important to notice that Eq. (5.2) does not imply that  $A_0$  and  $A_4$  are both non-vanishing in the leading order limit.

Table 3 summarizes the angular dependence of the squared amplitude at leading order in  $\alpha_S$  arising from the SM and the different dimension-6 operators that we consider. In particular, we immediately see that the contributions proportional to a linear combination of  $(1 - \cos \theta)^2$  and  $(1 + \cos \theta)^2$  can only arise from Eq. (5.2) if  $A_0 = 0$ . This is the Lam-Tung relation at order  $\mathcal{O}(\alpha_S^0)$ :

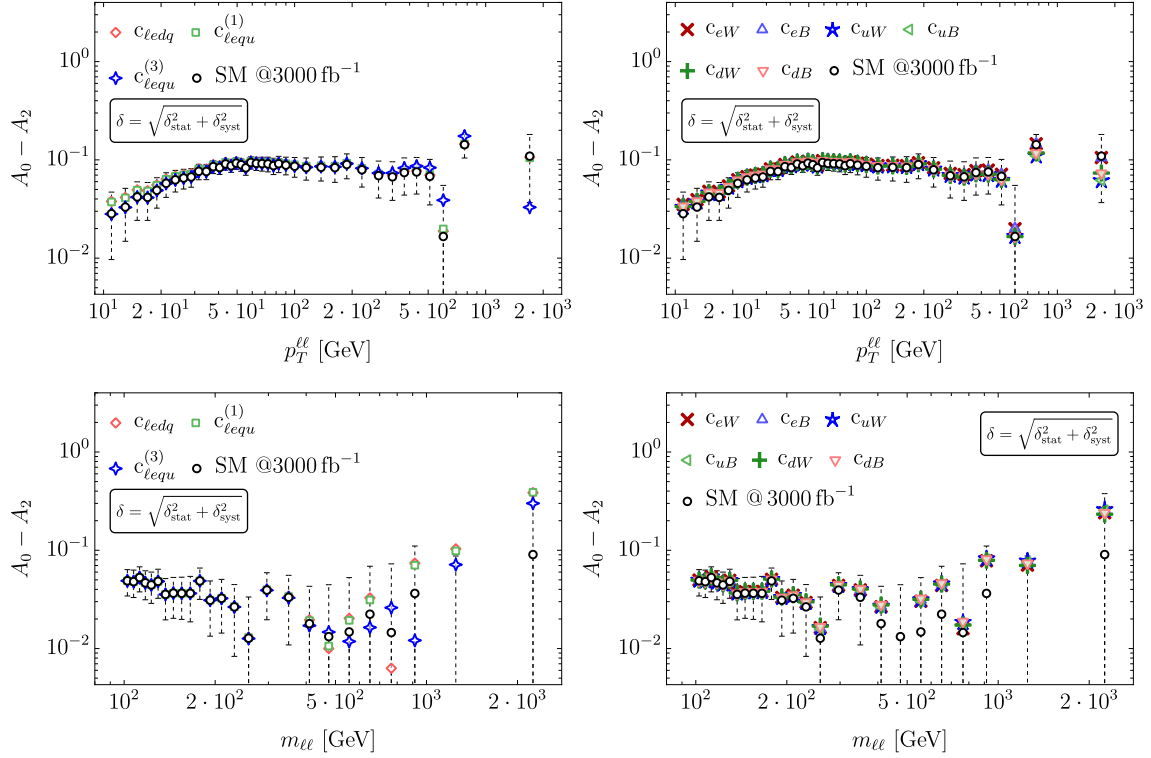
$$\lim_{\alpha_S \rightarrow 0} (A_0 - A_2) = A_0 = A_2 = 0. \quad (5.3)$$

Table 3 also shows that the only operators that can break this relation at order  $\mathcal{O}(\alpha_S^0)$  are the dipole operators  $\mathcal{O}_{(3)}$  and the chirality-breaking scalar/tensor four-fermion operators  $\mathcal{O}_{(8)}$  with angular dependences respectively proportional to  $1 - \cos^2 \theta$  and to a constant term.

## 5.2 Lam-Tung relation breaking at $\mathcal{O}(\alpha_S)$

At  $\mathcal{O}(\alpha_S)$  the SM does not violate the Lam-Tung relation as a consequence of the fact that gluons couple to the vector quark current, as explained in details in Ref. [52]. This implies that four-fermion operators involving the vector quark current (namely  $\mathcal{O}_{(5,6,7)}$ , following the notation in Table 3) can not violate the Lam-Tung relation. As already mentioned in Section 1, the effect of the operators  $\mathcal{O}_{(1,2,4)}$  does not grow with energy and can safely be

<sup>8</sup>The additional factor  $1/(2\pi)$  appearing in Eq. (2.1) has been absorbed by the integral over  $\phi$ .



**Figure 4:** Comparison between the contribution of the different SMEFT operators to the transverse momentum (first row) and invariant mass distribution (second row) of the  $A_0 - A_2$  observable. The left column shows scalar/tensor four-fermion operators, the right one shows the dipole operators. For each distribution, the Wilson coefficients are fixed equal to the largest positive value consistent with the bounds from the corresponding kinematic distribution at  $3000 \text{ fb}^{-1}$  (Table 4 for  $p_T^{\ell\ell}$  and Table 5 for  $m_{\ell\ell}$ ).

neglected.<sup>9</sup> Thus, even at order  $\mathcal{O}(\alpha_S)$ , the only operators expected to give an observable Lam-Tung breaking effect are the dipole and the scalar/tensor four-fermion operators. The  $\mathcal{O}(\alpha_S)$  contributions of these operators to the  $A_0 - A_2$  observable is compared to the first non-vanishing SM contribution (corresponding to  $\mathcal{O}(\alpha_S^2)$ ) in Figure 4. The SM curves are the same as those shown in Figures 2 and 3, while the SMEFT contributions are computed at order  $\mathcal{O}(\alpha_S)$ , for Wilson coefficients fixed to the  $3000 \text{ fb}^{-1}$  (positive) exclusion bound reported in Tables 4 and 5 (see Section 6 for details on how these bounds are derived).

## 6 Analysis and projected limits

In this section, we detail the procedure used to extract the projected constraints on the Wilson coefficient appearing in Eq. (1.2), and we specify the hypotheses underlying our analysis.

We considered, at the LHC, a center-of-mass energy of 13 TeV and two benchmark integrated luminosities:  $300 \text{ fb}^{-1}$ , corresponding approximately to the dataset expected

<sup>9</sup>One could expect that contributions to the Drell-Yan process from the  $s$ -channel Higgs boson exchange could break Lam-Tung already at  $\mathcal{O}(\alpha_S^0)$ . However, even if they did, these contributions are too small to be observed.

by the end of Run 3, and  $3000 \text{ fb}^{-1}$ , representative of the High-Luminosity LHC (HL-LHC) scenario. Since measurements of  $A_0 - A_2$  at 13 TeV are not yet available, we rely on simulations to obtain pseudo-data, as specified in Section 2. These simulations are performed under the SM-only hypothesis for the process  $pp \rightarrow \ell^+ \ell^- + X$  at next-to-next-to-leading order (NNLO) in QCD, *i.e.*, at  $\mathcal{O}(\alpha_S^2)$ , using the `MinNLOPS` framework. The resulting predictions are treated as pseudo-data for the purpose of our projections, with uncertainties estimated as explained in Section 2.1. Predictions for the  $A_0 - A_2$  observable in the SMEFT framework have been calculated analytically as explained in Section 2 and are expressed as functions of  $c_{\text{NP}}^2/\Lambda^4$ , where  $c_{\text{NP}}^2$  generically denotes the square of a Wilson coefficient of those appearing in Eq. (1.2).

The  $A_0 - A_2$  observable in the presence of NP contributions can be expressed as:

$$(A_0 - A_2)^{\text{SMEFT}} = 4 - 10 \left[ \frac{\int d\sigma^{\text{SM}}(\cos \theta, \phi, m_{\ell\ell}, p_T^{\ell\ell}) d\cos \theta d\phi (\cos^2 \theta + \sin^2 \theta \cos 2\phi)}{d\sigma^{\text{SM}}(m_{\ell\ell}, p_T^{\ell\ell}) + \left(\frac{c_{\text{NP}}}{\Lambda^2}\right)^2 d\tilde{\sigma}^{\text{NP}}(m_{\ell\ell}, p_T^{\ell\ell})} + \left(\frac{c_{\text{NP}}}{\Lambda^2}\right)^2 \frac{\int d\tilde{\sigma}^{\text{NP}}(\cos \theta, \phi, m_{\ell\ell}, p_T^{\ell\ell}) d\cos \theta d\phi (\cos^2 \theta + \sin^2 \theta \cos 2\phi)}{d\sigma^{\text{SM}}(m_{\ell\ell}, p_T^{\ell\ell}) + \left(\frac{c_{\text{NP}}}{\Lambda^2}\right)^2 d\tilde{\sigma}^{\text{NP}}(m_{\ell\ell}, p_T^{\ell\ell})} \right]. \quad (6.1)$$

Due to the NP contribution appearing in the denominator, the dependence of  $(A_0 - A_2)^{\text{SMEFT}}$  on the Wilson coefficient is non-linear, as anticipated above, and also affects the normalization of the distribution. This is expected to potentially break the Gaussian assumption that would allow a straightforward  $\chi^2$  analysis. For this reason, we decided to extract the bounds using the log-likelihood-ratio (LLR) test-statistic, which represents a more robust procedure for non-linear  $\chi^2$  (non-Gaussian likelihood). The LLR is defined as:

$$t_c = -2 \ln \frac{\mathcal{L}_{H_0}}{\mathcal{L}_{H_1}(\mathbf{c})}, \quad (6.2)$$

where, generically,  $H_0$  represents the null hypothesis and  $H_1$  the alternative hypothesis, that depends on some parameters  $\mathbf{c}$ . In our specific case,  $H_0$  is the SM-only hypothesis,  $H_1$  the SMEFT hypothesis, and the  $\mathbf{c}$  parameters are the relevant Wilson coefficients. For the two hypotheses, we assumed:

- bin-by-bin, the likelihood for the SM hypothesis is considered to be a gaussian distribution, centered around the  $A_0 - A_2$  central value provided by the simulations, with a width fixed by the estimated uncertainty. The total likelihood is then:

$$\mathcal{L}_{H_0} = \prod_{i=1}^{n_{\text{bins}}} N((A_0 - A_2)_i^{\text{SM}}; \sigma_i). \quad (6.3)$$

- analogously, the likelihood for the SMEFT hypothesis is constructed as the product of gaussian distributions that, bin-by-bin, are centered around the  $(A_0 - A_2)^{\text{SMEFT}}$  central value, calculated as explained above, with the same variance as in the SM-only

hypothesis:<sup>10</sup>

$$\mathcal{L}_{H_1}(c_{\text{NP}}) = \prod_{i=1}^{n_{\text{bins}}} N((A_0 - A_2)_i^{\text{SMEFT}}(c_{\text{NP}}); \sigma_i) , \quad (6.4)$$

where we have made explicit the  $(A_0 - A_2)^{\text{SMEFT}}$  dependence on the Wilson coefficients.

Each Wilson coefficient is constrained individually by setting all others to zero.<sup>11</sup> The analysis is performed using two kinematic distributions: the transverse momentum of the lepton pair  $p_T^{\ell\ell}$  for above  $p_T^{\ell\ell} > 10$  GeV and  $80 \text{ GeV} < m_{\ell\ell} < 100$  GeV, and the di-lepton invariant mass  $m_{\ell\ell}$  for above  $m_{\ell\ell} > 100$  GeV and  $p_T^{\ell\ell} > 10$  GeV. The binning schemes adopted for both cases are provided in Tables 8-15 of Appendix E, and are inspired by the existing measurements of Refs. [41, 43].

To constrain each Wilson coefficient, we estimated the distribution of the test-statistic  $t_{c_{\text{NP}}}$  under the SM hypothesis  $H_0$ , for a fixed, reasonable, initial value of  $c_{\text{NP}}$ , by computing its value on  $10^4$  pseudo-experiments drawn from  $\mathcal{L}_{H_0}$ . More explicitly, we used the available Monte Carlo to draw, with replacement, pseudo-data and used them to compute  $t_{c_{\text{NP}}}$   $10^4$  times. This yields a distribution of values of  $t_{c_{\text{NP}}}$ . From this distribution we can identify a threshold, denoted by  $\bar{t}_{c_{\text{NP}}}$ , defining the 95% confidence level (CL) threshold for rejecting the null hypothesis  $H_0$  when testing against the alternative hypothesis  $H_1$  corresponding to the fixed value  $c_{\text{NP}}$ .

Next, we compute the average value of  $t_{c_{\text{NP}}}$  over  $10^3$  samples drawn from  $\mathcal{L}_{H_1}$ . This corresponds to generating pseudo-experiments corresponding to the  $H_1$  hypothesis with fixed  $c_{\text{NP}}$ , computing  $t_{c_{\text{NP}}}$  for each of these pseudo-experiments, and taking the average.<sup>12</sup> The corresponding average value is denoted by  $t_{c_{\text{NP}}}^*$ .

Finally, both the threshold value  $\bar{t}_{c_{\text{NP}}}$  and the average value  $t_{c_{\text{NP}}}^*$  are iteratively computed adjusting the value of  $c_{\text{NP}}$  (using a bisection method) until they are equal, within a fixed threshold

$$\delta_{c_{\text{NP}}} = 2 \left| \frac{t_{c_{\text{NP}}}^* - \bar{t}_{c_{\text{NP}}}}{t_{c_{\text{NP}}}^* + \bar{t}_{c_{\text{NP}}}} \right| , \quad \text{with } \delta_{c_{\text{NP}}} < 5\% . \quad (6.5)$$

This is equivalent to solving the optimization problem:

$$\tilde{c}_{\text{NP}} = \arg \min_{c_{\text{NP}}} |\delta_{c_{\text{NP}}} - 5\%| . \quad (6.6)$$

where  $\tilde{c}_{\text{NP}}$  represents the Wilson coefficient value corresponding to the 95% CL bound.

<sup>10</sup>Here we assume that the uncertainty is not significantly affected by the presence of NP contributions. This is a reasonable assumption, which can possibly be relaxed, if needed, by assuming  $\sigma_i = \sigma_i(c_{\text{NP}})$  in Eq. (6.4).

<sup>11</sup>Obviously, since we have an implementation of the full likelihood in Eq. (6.4), we could also perform a simultaneous fit of some, or all coefficients, or a combination with other analyses.

<sup>12</sup>Comparing the average test-statistic under the alternative hypothesis with the distribution of the test-statistic under the null hypothesis is one possible procedure to compute a bound. Another option would be to compute the full distribution under the alternative hypothesis and compare the two distributions in terms of a “confusion matrix”, or to require a given power of the test at fixed CL. These are arbitrary choices of hypothesis testing.

95%CL, $\Lambda = 4$ TeV $p_T^{\ell\ell}$ distribution	$\mathcal{L} = 300 \text{ fb}^{-1}$		$\mathcal{L} = 3000 \text{ fb}^{-1}$	
	$A_0 - A_2$	cross-section	$A_0 - A_2$	cross-section
$c_{\ell equ}^{(3)}$	[-19.1, 19.1]	[-15.6, 15.8]	[-12.9, 13]	[-14.1, 14.1]
$c_{\ell equ}^{(1)}$	[-352, 344]	[-363, 359]	[-346, 344]	[-359, 359]
$c_{\ell edq}$	[-388, 375]	[-400, 400]	[-375, 375]	[-400, 400]
$c_{eW}$	[-9.61, 9.61]	[-18, 17.6]	[-9.38, 9.38]	[-17.2, 17.2]
$c_{eB}$	[-17.5, 17.5]	[-32.8, 32]	[-17.5, 17.5]	[-32, 32]
$c_{uW}$	[-13.1, 13.4]	[-3.2, 3.28]	[-11.4, 11.6]	[-2.85, 2.86]
$c_{uB}$	[-23.8, 23.8]	[-5.63, 5.78]	[-20.9, 20.6]	[-5.16, 5.16]
$c_{dW}$	[-14.4, 14.4]	[-4.45, 4.42]	[-13.1, 13.1]	[-3.98, 3.98]
$c_{dB}$	[-25.8, 25.8]	[-7.97, 7.97]	[-23.4, 23.8]	[-7.03, 7.03]

**Table 4:** 95% CL individual bounds for the Wilson coefficients in Eq. (1.2) for integrated luminosity values of  $300 \text{ fb}^{-1}$  and  $3000 \text{ fb}^{-1}$ . For each luminosity value, in the left column are reported the bounds obtained looking at the  $A_0 - A_2$  observable and in the right column are reported the bounds obtained looking at the cross-section in the  $p_T^{\ell\ell}$  distribution, fixing the NP scale  $\Lambda$  as  $\Lambda = 4$  TeV.

95%CL, $\Lambda = 4$ TeV $m_{\ell\ell}$ distribution	$\mathcal{L} = 300 \text{ fb}^{-1}$		$\mathcal{L} = 3000 \text{ fb}^{-1}$	
	$A_0 - A_2$	cross-section	$A_0 - A_2$	cross-section
$c_{\ell equ}^{(3)}$	[-0.297, 0.289]	[-0.0641, 0.0645]	[-0.141, 0.141]	[-0.0645, 0.0625]
$c_{\ell equ}^{(1)}$	[-1.64, 1.62]	[-0.152, 0.15]	[-0.703, 0.703]	[-0.149, 0.148]
$c_{\ell edq}$	[-2.11, 2.19]	[-0.205, 0.202]	[-0.898, 0.938]	[-0.199, 0.199]
$c_{eW}$	[-5.63, 5.63]	[-2.34, 2.34]	[-3.31, 3.28]	[-2.34, 2.29]
$c_{eB}$	[-9.38, 9.06]	[-3.63, 3.59]	[-5.31, 5.42]	[-3.59, 3.63]
$c_{uW}$	[-7.24, 7.27]	[-2.87, 2.86]	[-4.22, 4.34]	[-2.93, 2.81]
$c_{uB}$	[-6.09, 6.09]	[-2.34, 2.37]	[-3.57, 3.52]	[-2.34, 2.34]
$c_{dW}$	[-8.67, 8.91]	[-3.81, 3.84]	[-5.33, 5.33]	[-3.87, 3.87]
$c_{dB}$	[-7.59, 7.31]	[-3.13, 3.16]	[-4.5, 4.5]	[-3.17, 3.13]

**Table 5:** 95% CL individual bounds for the Wilson coefficients in Eq. (1.2) for integrated luminosity values of  $300 \text{ fb}^{-1}$  and  $3000 \text{ fb}^{-1}$ . For each luminosity value, in the left column are reported the bounds obtained looking at the  $A_0 - A_2$  observable and in the right column are reported the bounds obtained looking at the cross-section in the  $m_{\ell\ell}$  distribution, fixing the New Physics scale  $\Lambda$  as  $\Lambda = 4$  TeV.

This procedure is carried out to obtain both the upper and the lower bounds. Since NP contributions manifest themselves as  $c_{\text{NP}}^2/\Lambda^4$  and uncertainties are symmetric, the resulting constraints are expected to be symmetric around zero. Nevertheless, we extract both sides independently.<sup>13</sup> Results are presented and discussed in the next section.

## 7 Results and discussion

In Tables 4 and 5 we report the 95% CL individual bounds for all the Wilson coefficients in Eq. (1.2), equally valid for both electrons and muons, fixing the NP scale to  $\Lambda = 4$  TeV. For the  $m_{\ell\ell}$  analysis, the last bin, corresponding to  $3 - 10$  TeV, was not included because the estimated uncertainty was too large, and the region was partly outside of EFT validity range. For each luminosity value, we also report, for comparison, the bounds

<sup>13</sup>In some cases the bounds on certain Wilson coefficients are not exactly symmetric. These small deviations arise from small numerical instabilities in the procedure used to estimate the LLR distribution and give an idea of the uncertainty in our numerical optimization procedure.



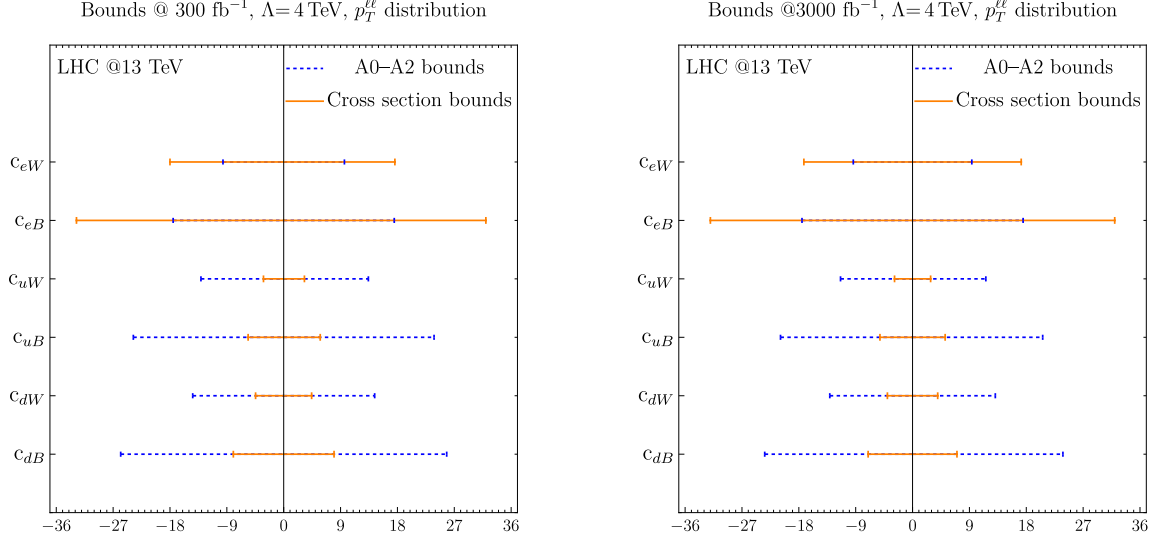


**Figure 5:** Comparison between the 95% CL boundaries obtained looking at the  $A_0 - A_2$  observable (blue) and the cross-section (orange) in the  $p_T^{\ell\ell}$  distribution. Left:  $300 \text{ fb}^{-1}$ . Right:  $3000 \text{ fb}^{-1}$

obtained from the differential cross-sections. The procedure to extract the latter bounds is the same as the one described above, except that the  $A_0 - A_2$  observable is replaced by the corresponding differential cross-section. Results in Tables 4 and 5 are obtained considering two benchmark values for the integrated luminosity, corresponding to  $300 \text{ fb}^{-1}$  and  $3000 \text{ fb}^{-1}$ . We have fixed the NP scale to  $\Lambda = 4 \text{ TeV}$ , and we focused on the  $A_0 - A_2$  observable and on the  $p_T^{\ell\ell}$  and  $m_{\ell\ell}$  differential cross-sections.

For a more immediate visual comparison, the same bounds, except for the four-fermion operators in the  $p_T^{\ell\ell}$  distribution, are shown graphically in Figures 5 and 6. We have not included the constraints on the Wilson coefficient of the four-fermion operators in Figure 5, since the  $p_T^{\ell\ell}$  distribution does not provide reasonably stringent bounds on them.<sup>14</sup>

Comparing the bounds shows that, in general, the constraints are tighter when looking at the cross-section rather than  $A_0 - A_2$  observable (see Appendix D for an intuitive explanation). However, our analysis neglects the leading operators contributing to the cross-section, namely the current-current operators that interfere with the SM. In an analysis including all operators, those in Eq. (1.2) would be sub-leading and thus extremely hard to constrain. The  $A_0 - A_2$  observable, on the other-hand, offers a complementary channel where the contribution of the current-current operators is highly suppressed, thanks to the interference with the SM and the Lam-Tung relation, and the dipole and scalar and tensor four-fermions operators provide the leading contributions. In the spirit of global fits and of breaking degeneracies between different (classes of) operators, the  $A_0 - A_2$  observable becomes a very valuable tool, which gives independent and direct access to the chirality-breaking operators.

From Tables 4 and 5, we can also see that the bounds projected for  $300 \text{ fb}^{-1}$  and for

<sup>14</sup>This is due to the fact that the  $p_T^{\ell\ell}$  analysis is done in a small window around the  $Z$  mass peak ( $80 \text{ GeV} < m_{\ell\ell} < 100 \text{ GeV}$ ), where the four-fermion operators do not profit of the Breit-Wigner enhancement of contributions involving the  $Z$  boson propagator.

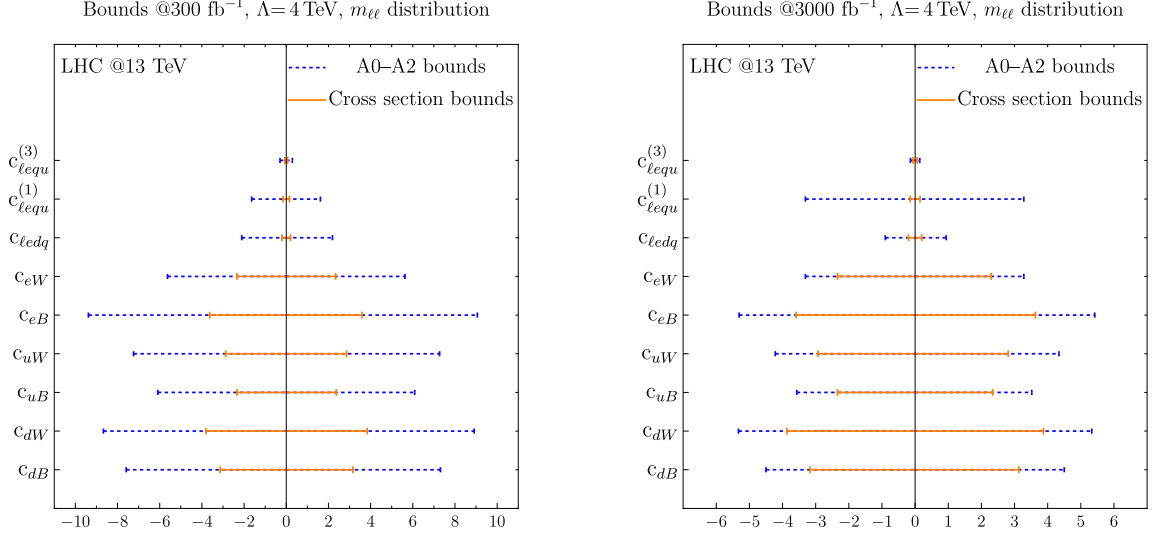


**Figure 6:** Comparison between the 95% CL boundaries obtained looking at the  $A_0 - A_2$  observable (blue) and the cross-section (orange) in the  $m_{\ell\ell}$  distribution. Left: 300 fb<sup>-1</sup>. Right: 3000 fb<sup>-1</sup>.

3000 fb<sup>-1</sup> are often comparable. This effect is more pronounced in the  $p_T^{\ell\ell}$  analysis and for the differential cross-section observable. This behavior comes from the fact that the bound on those coefficients is dominated by the systematic uncertainty, which we assume not to improve with luminosity. As we discussed before, systematic uncertainty dominate the low- $p_T$  and low- $m_{\ell\ell}$  regions, so that only operators with a shape significantly different from the SM in the high- $p_T$  or high- $m_{\ell\ell}$  regions will see a reasonable improvement in their bounds when increasing the integrated luminosity. The different shapes shown in Figure 4 confirm this interpretation and show that the different growth in energy of the dipole and four-fermion operators leads not only to different sensitivities in the two kinematic distributions, but also to a different pattern of improvement of the bounds with the integrated luminosity.

As mentioned above, the  $m_{\ell\ell}$  distribution, yields tighter bounds than the  $p_T^{\ell\ell}$  distribution, indicating that higher energies enhance the sensitivity to both classes of operators. This can be seen very neatly in Figure 6, which makes apparent how the four-fermion operators are more tightly constrained than the dipole ones.

Finally, in Tables 6 and 7, we report the bounds obtained using the Taylor expansion of the  $A_0 - A_2$  observable truncated at order  $c_{\text{NP}}^2/\Lambda^4$ . Such bounds do not differ significantly from those obtained using the full expression in Table 4 and 5. This is the expected behavior in the region of validity of the EFT expansion, where higher-order terms are sub-leading corrections. In particular, the expansion parameter involves the ratio  $d\sigma^{\text{SMEFT}}/d\sigma^{\text{SM}} \times (c_{\text{NP}}/\Lambda^2)^2$ , which remains sufficiently small for small enough Wilson coefficients and in most of the allowed phase space. The largest discrepancies between the two approaches appear in the regions of the phase space where the NP contributions are more significant, such as the tails of  $p_T^{\ell\ell}$  and  $m_{\ell\ell}$  distributions. In those regions, for relatively large values of the Wilson coefficients, the expansion parameter may become largish, making the expansion less reliable, and one could expect higher-order terms to become relevant. This is the

95% CL, $\Lambda = 4$ TeV $p_T^{\ell\ell}$ distribution	$\mathcal{L} = 300 \text{ fb}^{-1}$	$\mathcal{L} = 3000 \text{ fb}^{-1}$
$c_{lequ}^{(3)}$	$[-18.8, 18.8]$	$[-12.9, 12.8]$
$c_{lequ}^{(1)}$	$[-359, 348]$	$[-344, 344]$
$c_{ledq}$	$[-388, 375]$	$[-375, 375]$
$c_{eW}$	$[-9.38, 9.38]$	$[-9.38, 9.3]$
$c_{eB}$	$[-17.5, 17.5]$	$[-17.2, 16.9]$
$c_{uW}$	$[-12.6, 12.5]$	$[-10.4, 10.3]$
$c_{uB}$	$[-23.1, 23.1]$	$[-18.9, 19.2]$
$c_{dW}$	$[-14.1, 14.1]$	$[-12.5, 12.5]$
$c_{dB}$	$[-25, 25.4]$	$[-22.7, 22.7]$

**Table 6:** 95% CL individual bounds for the Wilson coefficients in eq. 1.2 for integrated luminosity values of  $300 \text{ fb}^{-1}$  and  $3000 \text{ fb}^{-1}$ . These are obtained looking at the  $A_0 - A_2$  observable in the  $p_T$  distribution expanded at order  $c_{\text{NP}}^2/\Lambda^4$ , fixing the New Physics scale  $\Lambda$  as  $\Lambda = 4$  TeV.

95% CL, $\Lambda = 4$ TeV $m_{\ell\ell}$ distribution	$\mathcal{L} = 300 \text{ fb}^{-1}$	$\mathcal{L} = 3000 \text{ fb}^{-1}$
$c_{lequ}^{(3)}$	$[-0.227, 0.234]$	$[-0.133, 0.129]$
$c_{lequ}^{(1)}$	$[-1, 0.988]$	$[-0.563, 0.568]$
$c_{ledq}$	$[-1.31, 1.31]$	$[-0.738, 0.75]$
$c_{eW}$	$[-5.47, 5.31]$	$[-3.32, 3.28]$
$c_{eB}$	$[-8.75, 8.75]$	$[-5.31, 5.31]$
$c_{uW}$	$[-7.03, 7.03]$	$[-4.16, 4.24]$
$c_{uB}$	$[-6.04, 5.86]$	$[-3.52, 3.52]$
$c_{dW}$	$[-8.44, 8.44]$	$[-5.27, 5.27]$
$c_{dB}$	$[-7.03, 7.23]$	$[-4.45, 4.45]$

**Table 7:** 95% CL individual bounds for the Wilson coefficients in Eq. 1.2 for integrated luminosity values of  $300 \text{ fb}^{-1}$  and  $3000 \text{ fb}^{-1}$ . These are obtained looking at the  $A_0 - A_2$  observable in the  $m_{\ell\ell}$  distribution expanded at order  $c_{\text{NP}}^2/\Lambda^4$ , fixing the New Physics scale  $\Lambda$  as  $\Lambda = 4$  TeV.

reason why we believe that showing both sets of bounds is useful, as it gives an idea of the robustness of the results.

## 8 Conclusions

In this work, we analyzed the contributions of chirality-breaking dimension-six operators, specifically dipole and four-fermion operators, to the Drell–Yan (DY) process.

Our focus was on the angular observable  $A_0 - A_2$ , which vanishes in the Standard Model (SM) up to  $\mathcal{O}(\alpha_S^2)$  and does not receive contributions from dimension-six operators that interfere with the SM amplitude. In Ref. [9], bounds on dipole operators were derived at a center-of-mass energy of 8 TeV using the ATLAS analysis of Ref. [48]. Here, we extended that study by providing projected bounds at 13 TeV, considering both dipole and four-fermion operators, and using both the  $p_T^{\ell\ell}$  and  $m_{\ell\ell}$  distributions.

We performed SM Monte Carlo simulations at  $\mathcal{O}(\alpha_S^2)$  with the `MiNNLOPS` tool, and included the NP contributions analytically to estimate their effect on the  $p_T^{\ell\ell}$  and  $m_{\ell\ell}$  distributions of the DY cross-section, the angular coefficients  $A_\ell$ , and the  $A_0 - A_2$  observable. A pseudo-analysis was carried out for  $300 \text{ fb}^{-1}$  of integrated luminosity, corresponding to the final LHC dataset, and for  $3000 \text{ fb}^{-1}$  of integrated luminosity, corresponding to the HL-LHC. We included estimates of both theoretical and experimental systematic uncertainties, based on current measurements and projections for future improvements.

We compared the 95% CL bounds on Wilson coefficients extracted from  $A_0 - A_2$  with those obtained from the differential cross-section. The latter are found to be generally more stringent, which is not surprising given the much larger statistics and smaller experimental uncertainties available for cross-section measurements. However, the key point of this work is that the angular observable  $A_0 - A_2$  offers a clean and independent probe of chirality-breaking operators, free from contamination by dimension-six operators that interfere with the SM. This is not the case for the cross-section, where SM contributions are never suppressed and the leading SMEFT effects arise from interference with current-current four-fermion operators. As such,  $A_0 - A_2$  becomes particularly valuable in global SMEFT fits, where multiple operators are constrained simultaneously and degeneracies in parameter space must be resolved.

We stress that our study was conducted in a simplified theoretical setup and does not attempt to replicate a full experimental analysis. In particular, we assumed direct access to the angular coefficients and to the  $A_0 - A_2$  observable, whereas real analyses typically extract these quantities via template fits. While we strived to provide realistic estimates of theoretical and experimental systematics, a dedicated experimental study will ultimately be required to fully assess the potential of  $A_0 - A_2$  for probing chirality-breaking SMEFT operators at the LHC.

## Acknowledgements

X.L. is grateful to Bin Yan for early collaboration on the project and for useful discussions. R.T. thanks Emanuele Re for help with the `POWHEG` and `MiNNLOPS` codes. We thank R. Rattazzi for comments on the UV origin of the chirality-breaking operators. We also thank the INFN Genova IT department for continuous support with the computing resources.

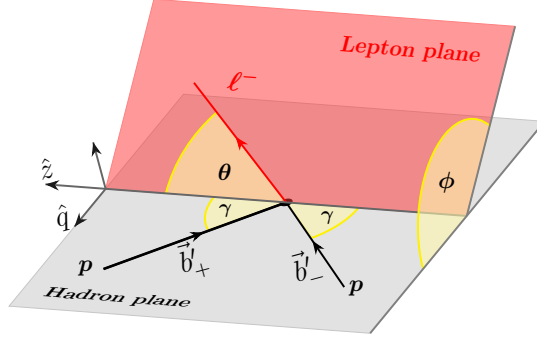


**Figure 7:** A graphic representation of the Collins-Soper frame.

## A The Collins-Soper frame

Let the 4-vectors of the two incident beams in the laboratory frame be:

$$b_+ = (E_{b_+}, \vec{b}_+), \quad (\text{A.1})$$

$$b_- = (E_{b_-}, \vec{b}_-). \quad (\text{A.2})$$

We call  $b'_+$  and  $b'_-$  the respective 4-vectors boosted in the di-lepton rest frame. The  $z$  axis of the CS frame is defined as the bisector of the unit vectors  $\hat{b}'_+$  and  $-\hat{b}'_-$ , pointing such that its scalar product with the di-lepton 3-momentum, in the laboratory frame, is positive.

Another axis, called  $q$ , is defined as the one laying in the plane defined by  $\hat{b}'_+$  and  $\hat{b}'_-$ , orthogonal to the  $z$  axis and pointing in the direction opposite to  $\hat{b}'_+ + \hat{b}'_-$ .

The angle  $\theta$  is defined with respect to the  $z$  axis, while the angle  $\phi$  is defined with respect to the  $q$  axis.

This orientation of the CS frame axes can provide, for certain events, angles that are shifted by  $\pi$  with respect to those defined in the original paper [17]. This can be taken into account by slightly modifying the original definitions, introducing a factor  $p_z^{\ell\ell} / |p_z^{\ell\ell}|$  that accounts for axis orientation. Therefore, one has:

$$\cos \theta = \frac{p_{z,\ell\ell}}{|p_{z,\ell\ell}|} \frac{2(p_{z,\ell^+} E_{\ell^-} - p_{z,\ell^-} E_{\ell^+})}{m_{\ell\ell} \sqrt{m_{\ell\ell}^2 + p_T^{\ell\ell}}} \quad (\text{A.3})$$

$$\tan \phi = \frac{p_{z,\ell\ell}}{|p_{z,\ell\ell}|} \frac{\sqrt{m_{\ell\ell}^2 + p_{T,\ell\ell}^2}}{m_{\ell\ell}} \frac{\Delta p_T^{\ell\ell} \cdot \hat{R}_T}{\Delta p_T^{\ell\ell} \cdot \hat{p}_{T,\ell\ell}} \quad (\text{A.4})$$

where  $\hat{p}_{T,\ell\ell}$  is a unit vector in the direction of  $p_T^{\ell\ell}$  and  $\hat{R}_T$  is the normalized cross product between  $\hat{b}'_+$  and  $p_{z,\ell\ell}$ .

## B Angular observables from spherical-harmonics

In the following, we report the combination of spherical harmonics that provides the factor multiplying each  $A_l$  in Eq. (2.1).

$$\begin{aligned}
1 + \cos^2 \theta &= \frac{4\sqrt{\pi}}{15} \left( 10Y_0^0 + \sqrt{5}Y_2^0 \right), \\
\frac{1}{2}(1 - 3\cos^2 \theta) &= -2\sqrt{\frac{\pi}{5}}Y_2^0, \\
\sin 2\theta \cos \phi &= 2\sqrt{\frac{2\pi}{15}}(Y_2^{-1} - Y_2^1), \\
\frac{1}{2}(\sin^2 \theta \cos 2\phi) &= \sqrt{\frac{2\pi}{15}}(Y_2^{-2} + Y_2^2), \\
\sin \theta \cos \phi &= \sqrt{\frac{2\pi}{3}}(Y_1^{-1} - Y_1^1), \\
\cos \theta &= 2\sqrt{\frac{\pi}{3}}Y_1^0, \\
\sin^2 \theta \sin 2\phi &= -2i\sqrt{\frac{2\pi}{15}}(Y_2^{-2} - Y_2^2), \\
\sin 2\theta \sin \phi &= -2i\sqrt{\frac{2\pi}{15}}(Y_2^{-1} + Y_2^1), \\
\sin \theta \sin \phi &= -i\sqrt{\frac{2\pi}{3}}(Y_1^{-1} + Y_1^1).
\end{aligned}$$

One can verify that, apart from the first two, each of these combinations of spherical harmonics is orthogonal to the others.

## C Differential cross-section and PDF integration

In this appendix we derive the expression for the fully differential unpolarized cross-section for the process  $pp \rightarrow \ell^+ \ell^- X$  at  $\mathcal{O}(\alpha_S)$ . This is achieved by splitting it in two subsequent processes: the first is  $pp \rightarrow ZX$ , which on the partonic level gives  $q\bar{q} \rightarrow Zg$  or  $qg \rightarrow Zq$ ; the second consists in the  $Z$  boson decaying into the lepton pair  $Z \rightarrow \ell^+ \ell^-$ . Neglecting the quark masses the kinematic constraint  $s + t + u = m_{\ell\ell}^2$  must hold, where  $m_{\ell\ell}$  denotes the invariant mass of the lepton pair and  $s, t$  and  $u$  the partonic Mandelstam variables defined for the first subprocess.

In the CS frame the  $Z$  boson momentum reads  $p_Z = (E_Z, p_T^{\ell\ell}, 0, p_l)$ . All the kinematic quantities are expressed in terms of:

- the invariant mass of the lepton pair  $m_{\ell\ell}$ ;
- the transverse momentum of the lepton pair  $p_T^{\ell\ell}$ ;
- the energy of each hadron in the laboratory frame  $E_p$ ;

- the rapidity  $y = \log \left( \frac{E_Z + p_l}{E_Z - p_l} \right)$  of the  $Z$  boson;
- the fraction of hadronic momentum carried by the incoming partons  $x_a$ .

In terms of these quantities, the energy  $E_Z$  and longitudinal momentum  $p_l$  become

$$E_Z = \sqrt{m_{\ell\ell}^2 + (p_T^{\ell\ell})^2} \cosh y, \quad p_l = \sqrt{m_{\ell\ell}^2 + (p_T^{\ell\ell})^2} \sinh y, \quad (\text{C.1})$$

and the Mandelstam variables can be rewritten as

$$s = 4x_a x_b E_p^2, \quad t = m_{\ell\ell}^2 - 2x_a E_p \sqrt{m_{\ell\ell}^2 + (p_T^{\ell\ell})^2} e^{-y}, \quad u = m_{\ell\ell}^2 - 2x_b E_p \sqrt{m_{\ell\ell}^2 + (p_T^{\ell\ell})^2} e^y. \quad (\text{C.2})$$

The general expression for the hadronic cross-section  $\sigma_{pp \rightarrow X \ell^+ \ell^-}$  is

$$\begin{aligned} \sigma_{pp \rightarrow X \ell^+ \ell^-} &= \sum_{ab} \int \frac{d^3 p_X}{(2\pi)^3 2E_X} \frac{d^3 p_{\ell^+}}{(2\pi)^3 2E_{\ell^+}} \frac{d^3 p_{\ell^-}}{(2\pi)^3 2E_{\ell^-}} \frac{1}{2s} f_{a/p}(x_a) f_{b/p}(x_b) dx_a dx_b \\ &\times \langle |\mathcal{M}_{ab}|^2 \rangle (2\pi)^4 \delta^{(4)}(p_a + p_b - p_X - p_{\ell^+} - p_{\ell^-}), \end{aligned} \quad (\text{C.3})$$

with  $\mathcal{M}_{ab}$  the amplitudes for the partonic processes; the meaning of the other symbols is understood. Momentum conservation gives

$$\begin{aligned} d\sigma_{pp \rightarrow X \ell^+ \ell^-} &= \sum_{ab} \int d^4 p_Z d\phi_{\ell\ell}^{(2)} \frac{d^3 p_X}{(2\pi)^3 2E_X} \frac{1}{2s} f_{a/p}(x_a) f_{b/p}(x_b) dx_a dx_b \\ &\times \langle |\mathcal{M}_{ab}|^2 \rangle (2\pi)^4 \delta^{(4)}(p_a + p_b - p_X - p_Z), \end{aligned} \quad (\text{C.4})$$

where

$$d\phi_{\ell\ell}^{(2)} \equiv (2\pi)^4 \delta^{(4)}(p_Z - p_{\ell^+} - p_{\ell^-}) \frac{d^3 p_{\ell^+}}{(2\pi)^3 2E_{\ell^+}} \frac{d^3 p_{\ell^-}}{(2\pi)^3 2E_{\ell^-}} \quad (\text{C.5})$$

is the lepton pair phase space.

The integral on  $x_b$  is now performed using the identity  $\frac{d^3 p_X}{2E_X} = d^4 p_X \delta(p_X^2)$ : we can substitute in the Dirac  $\delta$ -function  $p_X^2 = s + t + u - m_{\ell\ell}^2$  and then use Eq. (C.2) to obtain

$$\delta(p_X^2) = \frac{1}{2E_p^2 |2x_a - x_T e^y|} \delta \left( x_b - \frac{x_a x_T e^{-y} - \frac{m_{\ell\ell}^2}{2E_p^2}}{2x_a - x_T e^y} \right), \quad (\text{C.6})$$

with  $x_T \equiv \sqrt{m_{\ell\ell}^2 + (p_T^{\ell\ell})^2}/E_p$ . Moreover, being  $x_b < 1$ , the above expression gives a lower limit on  $x_a$  that reads

$$x_a > x_a^{\min} \equiv \frac{x_T e^y - \frac{m_{\ell\ell}^2}{2E_p^2}}{2 - x_T e^{-y}}. \quad (\text{C.7})$$

The integration over the the lepton pair momenta gives

$$\sigma_{pp \rightarrow \ell^+ \ell^-} = \frac{1}{(2\pi)^6} \frac{1}{64E_p^4} \int \left[ \sum_{ab} \int_{x_a^{\min}}^1 f_{a/p}(x_a) f_{b/p}(x_b) dx_a \frac{\langle |\mathcal{M}_{ab}|^2 \rangle}{(2x_a - x_T e^y) x_a x_b^*} \right] dc_\theta d\phi d^4 p_Z, \quad (\text{C.8})$$

where the star in  $x_b^*$  keeps track of the constraint on  $x_b$  given by Eq. (C.6).

The 4-momentum of the outgoing  $Z$  boson can be parametrized as

$$p_Z = \left( \sqrt{m_{\ell\ell}^2 + (p_T^{\ell\ell})^2} \cosh y, p_T^{\ell\ell} \cos \alpha, p_T^{\ell\ell} \sin \alpha, \sqrt{m_{\ell\ell}^2 + (p_T^{\ell\ell})^2} \sinh y \right), \quad (\text{C.9})$$

which gives

$$d^4 p_Z = \frac{1}{2} p_T^{\ell\ell} d\alpha dm_{\ell\ell}^2 dp_T^{\ell\ell} dy. \quad (\text{C.10})$$

Plugging this into Eq. (C.8) and integrating over  $\alpha$  we find

$$\frac{d\sigma_{pp \rightarrow X\ell^+\ell^-}}{dm_{\ell\ell}^2 dp_T^{\ell\ell} dc_\theta d\phi} = \frac{1}{(2\pi)^5} \frac{\pi p_T^{\ell\ell}}{128 E_p^4} \int_{y_{\min}}^{y_{\max}} \left[ \sum_{ab} \int_{x_a^{\min}}^1 f_{a/p}(x_a) f_{b/p}(x_b^*) dx_a \frac{\langle |\mathcal{M}_{ab}|^2 \rangle}{(2x_a - x_T e^y) x_a x_b^*} \right] dy, \quad (\text{C.11})$$

where the upper and lower bounds

$$y_{\max} \equiv \log \left[ \frac{1}{2} \left( \frac{4E_p^2 + m_{\ell\ell}^2}{2E_p^2 x_T} + \sqrt{\left( \frac{4E_p^2 + m_{\ell\ell}^2}{2E_p^2 x_T} \right)^2 - 4} \right) \right], \quad (\text{C.12})$$

$$y_{\min} \equiv \log \left( \frac{x_T}{2} \right)$$

follow from the fact that  $x_a^{\min}$  is positive and lesser than 1.

The analytic results obtained using formula (C.11) were found to be in excellent agreement with those obtained with **Madgraph5** [53].

## D Cross-section vs $A_0 - A_2$ bounds

In this appendix, we provide an intuitive explanation for why the bounds obtained from the cross-section are tighter than those obtained with the  $A_0 - A_2$  observable. In particular we focus on the ratios:

$$r_1 = \left| \frac{\sigma^{\text{SMEFT}} - \sigma^{\text{SM}}}{\delta_{\sigma^{\text{SM}}}} \right|, \quad (\text{D.1})$$

$$r_2 = \left| \frac{(A_0 - A_2)^{\text{SMEFT}} - (A_0 - A_2)^{\text{SM}}}{\delta_{(A_0 - A_2)^{\text{SM}}}} \right|, \quad (\text{D.2})$$

$$R = \frac{r_1}{r_2}, \quad (\text{D.3})$$

where  $\delta_{\sigma^{\text{SM}}}$  and  $\delta_{(A_0 - A_2)^{\text{SM}}}$  indicate the uncertainty on the cross-section and the  $A_0 - A_2$  observable, respectively. Clearly, at fixed  $c_{\text{NP}}$ , a larger value of the ratio indicates that the corresponding observable is more sensitive to the considered operator. Figure 8 shows the  $r_1$  (upper left),  $r_2$  (upper right) and  $R$  (lower panel) ratios for the  $p_T^{\ell\ell}$  distribution with fixed luminosity of  $300 \text{ fb}^{-1}$ . Each Wilson coefficient  $c_{\text{NP}}$  is set to 10 and  $\Lambda$  is fixed at 4 TeV.



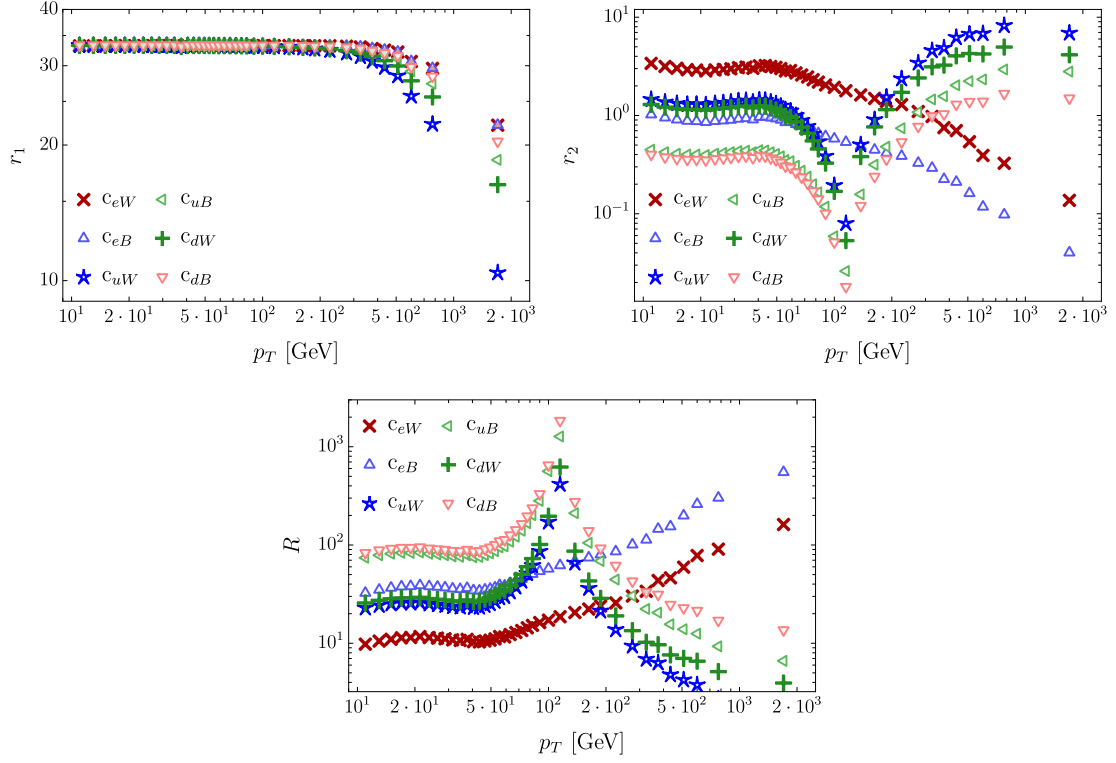


**Figure 8:** Plots of the ratios defined in equation (D.1) assuming  $\mathcal{L} = 300 \text{ fb}^{-1}$  in the  $p_T^{\ell\ell}$  distribution. Upper left:  $r_1$ , upper right:  $r_2$ , lower panel:  $R$ . The different behavior of  $c_{eW}$  and  $c_{eB}$ , that are better constrained by the  $A_0 - A_2$  observable, is evident.

It is immediate to notice that  $r_1$  is significantly larger than  $r_2$ , as  $R$  ranges from a few units up to more than 1000. This behavior indicates that the cross-section is more sensitive to NP insertion, due to its smaller uncertainties. Furthermore, the  $R$  plot shows a peak in the central bins, where  $A_0 - A_2$  increases and the statistical uncertainty is small thanks to the high statistics. This pattern does not occur for the  $c_{eW}$  and  $c_{eB}$  Wilson coefficients, which are, in fact, better constrained through the  $A_0 - A_2$  observable. An analogous behavior is observed for the  $3000 \text{ fb}^{-1}$  integrated luminosity. Similar conclusions hold when considering the  $m_{\ell\ell}$  distribution, where  $r_1$  remains consistently larger than  $r_2$ .

## E Numerical tables

In this appendix we report the numerical values of the observables appearing in Figures 1, 2, 3 with explicit separation of statistical and systematic uncertainties.

$p_T^{\ell\ell}$ [GeV]	$N_{\text{MC}}$	$\sigma$ [pb]	$\delta\sigma_{\text{stat}}^{300}$ [pb]	$\delta\sigma_{\text{stat}}^{3000}$ [pb]	$\delta\sigma_{\text{syst}}^{3\%}$ [pb]
10. – 12.	55355060	118.99	0.0462851	0.0146366	3.5697
12. – 14.	44432363	100.94	0.0350784	0.0110928	3.02821
14. – 16.	36325175	86.4391	0.0271705	0.00859205	2.59317
16. – 18.	30149734	74.566	0.0268787	0.00849979	2.23698
18. – 20.	25356520	64.7717	0.0211872	0.00669997	1.94315
20. – 22.5	26414219	69.6736	0.0345891	0.010938	2.09021
22.5 – 25.	21848818	59.3793	0.0205171	0.00648808	1.78138
25. – 27.5	18289822	51.0283	0.0207527	0.00656258	1.53085
27.5 – 30.	15450562	44.1082	0.0153048	0.00483982	1.32325
30. – 33.	15561084	45.4264	0.0155019	0.00490215	1.36279
33. – 36.	12982145	38.7237	0.0154616	0.00488938	1.16171
36. – 39.	10916808	33.2943	0.104793	0.0331385	0.99829
39. – 42.	9253016	28.593	0.0125402	0.00396556	0.857789
42. – 45.	7892013	24.7582	0.0112726	0.00356472	0.742747
45. – 48.	6768494	21.5125	0.0102497	0.00324124	0.645376
48. – 51.	5840548	18.7992	0.0102651	0.00324612	0.563975
51. – 54.	5053525	16.4331	0.009844	0.00311295	0.492994
54. – 57.	4394576	14.4348	0.0106579	0.00337034	0.433044
57. – 61.	5002474	16.5707	0.018601	0.00588215	0.497122
61. – 65.	4199710	14.0805	0.00805207	0.00254629	0.422415
65. – 70.	4330950	14.6711	0.0076631	0.00242328	0.440134
70. – 75.	3520638	12.0448	0.00867464	0.00274316	0.361345
75. – 80.	2883906	9.93928	0.00625729	0.00197873	0.298178
80. – 85.	2374827	8.24452	0.00648999	0.00205232	0.247335
85. – 95.	3608604	12.6469	0.021292	0.00673313	0.379406
95. – 105.	2524395	8.91138	0.00627343	0.00198383	0.267341
105. – 125.	3122264	11.1183	0.00677558	0.00214263	0.33355
125. – 150.	1999251	7.18747	0.00551796	0.00174493	0.215624
150. – 175.	1017474	3.68138	0.00427167	0.00135082	0.110441
175. – 200.	555846	2.01631	0.0030348	0.000959689	0.0604894
200. – 250.	518627	1.877	0.00313351	0.000990902	0.05631
250. – 300.	203615	0.735178	0.0018908	0.000597924	0.0220553
300. – 350.	89323	0.32241	0.00118899	0.000375991	0.00967229
350. – 400.	43580	0.156648	0.000841524	0.000266113	0.00469943
400. – 470.	28142	0.101251	0.000669394	0.000211681	0.00303754
470. – 550.	13814	0.0492041	0.000388475	0.000122847	0.00147612
550. – 650.	6735	0.0239324	0.000303223	0.0000958875	0.000717971
650. – 900.	4229	0.0148124	0.000228624	0.0000722974	0.000444371
900. – 2500.	791	0.00265501	0.0000894172	0.0000282762	0.0000796503

**Table 8:** Expected results of measurements of the transverse momentum spectrum at the LHC at 13 TeV with  $300 \text{ fb}^{-1}$  and  $3 \text{ ab}^{-1}$ . The columns show the bin range, the number of Monte Carlo events, the expected cross-section, the statistical uncertainty with  $300 \text{ fb}^{-1}$  and  $3 \text{ ab}^{-1}$ , and a systematic uncertainty of 3%.

$p_T^{\ell\ell}$ [GeV]	$A_0$	$(\delta A_0)_{\text{stat}}^{300}$	$(\delta A_0)_{\text{stat}}^{3000}$	$(\delta A_0)_{\text{syst}}^{3\%}$
10. – 12.	0.0454443	0.00114832	0.000363131	0.0186367
12. – 14.	0.0599507	0.00135674	0.000429039	0.0182015
14. – 16.	0.0762949	0.0014533	0.000459572	0.0177112
16. – 18.	0.0929306	0.00134978	0.000426839	0.0172121
18. – 20.	0.112002	0.0013841	0.000437691	0.01664
20. – 22.5	0.133622	0.001311	0.000414575	0.0159913
22.5 – 25.	0.158508	0.0011865	0.000375205	0.0152448
25. – 27.5	0.186841	0.00158303	0.000500597	0.0143948
27.5 – 30.	0.213909	0.00122356	0.000386924	0.0135827
30. – 33.	0.24182	0.00124103	0.000392448	0.0127454
33. – 36.	0.274575	0.0013978	0.000442023	0.0117627
36. – 39.	0.30449	0.00357953	0.00113195	0.0108653
39. – 42.	0.338655	0.00157738	0.00049881	0.00984036
42. – 45.	0.369891	0.00131081	0.000414515	0.00890328
45. – 48.	0.400941	0.00182146	0.000575997	0.00797177
48. – 51.	0.429686	0.00183945	0.000581685	0.00710942
51. – 54.	0.455141	0.00167453	0.000529532	0.00634577
54. – 57.	0.479131	0.00175029	0.00055349	0.00562608
57. – 61.	0.510621	0.00232018	0.000733707	0.00468139
61. – 65.	0.542085	0.00204103	0.000645431	0.00373744
65. – 70.	0.571995	0.00163757	0.000517846	0.00284015
70. – 75.	0.601204	0.00168406	0.000532546	0.00196388
75. – 80.	0.633106	0.00186528	0.000589854	0.00100681
80. – 85.	0.66316	0.00247316	0.000782083	0.0001052
85. – 95.	0.686713	0.0060731	0.00192048	0.000601351
95. – 105.	0.732296	0.00206278	0.000652307	0.00196888
105. – 125.	0.779334	0.00163382	0.000516661	0.00338001
125. – 150.	0.832182	0.0024437	0.000772765	0.00496547
150. – 175.	0.867126	0.00282857	0.000894471	0.00601376
175. – 200.	0.899789	0.0041151	0.00130131	0.00699372
200. – 250.	0.916585	0.00481605	0.00152297	0.00749755
250. – 300.	0.949971	0.00721618	0.00228196	0.00849908
300. – 350.	0.947089	0.0109943	0.00347669	0.00841257
350. – 400.	0.977413	0.0146018	0.0046175	0.0093229
400. – 470.	0.965547	0.0181728	0.00574673	0.00896602
470. – 550.	0.989361	0.0254853	0.00805915	0.00968054
550. – 650.	0.9903	0.0337669	0.010678	0.00970749
650. – 900.	0.978093	0.0496695	0.0157069	0.00934364
900. – 2500.	0.990086	0.111957	0.0354038	0.00968581

**Table 9:** Expected results of measurements of the  $A_0$  observable at the LHC at 13 TeV with 300 fb<sup>-1</sup> and 3 ab<sup>-1</sup>. The columns show the bin range, the expected value of  $A_0$ , the statistical uncertainty with 300 fb<sup>-1</sup> and 3 ab<sup>-1</sup>, and a systematic uncertainty of 3%.

$p_T^{\ell\ell}$ [GeV]	$A_2$	$(\delta A_2)_{\text{stat}}^{300}$	$(\delta A_2)_{\text{stat}}^{3000}$	$(\delta A_2)_{\text{syst}}^{3\%}$
10. – 12.	0.0236693	0.00121024	0.000382711	0.000710079
12. – 14.	0.0252714	0.00147315	0.000465851	0.000758143
14. – 16.	0.0305507	0.00105898	0.00033488	0.00091652
16. – 18.	0.0313687	0.00101226	0.000320105	0.00094106
18. – 20.	0.0379034	0.000984646	0.000311372	0.0011371
20. – 22.5	0.0410952	0.00108569	0.000343324	0.00123286
22.5 – 25.	0.045506	0.000973089	0.000307718	0.00136518
25. – 27.5	0.0499428	0.000975623	0.000308519	0.00149828
27.5 – 30.	0.0537455	0.00112234	0.000354915	0.00161236
30. – 33.	0.0579562	0.00105402	0.000333309	0.00173869
33. – 36.	0.0626439	0.00116594	0.000368703	0.00187932
36. – 39.	0.0598799	0.00623964	0.00197315	0.00179644
39. – 42.	0.0652713	0.00123154	0.000389449	0.00195814
42. – 45.	0.0695346	0.00134794	0.000426257	0.00208604
45. – 48.	0.070112	0.00140319	0.000443728	0.00210336
48. – 51.	0.0707345	0.00135741	0.000429251	0.00212204
51. – 54.	0.0727296	0.00144449	0.000456788	0.00218189
54. – 57.	0.0774697	0.00252136	0.000797325	0.00232409
57. – 61.	0.0773344	0.00353121	0.00111667	0.00232003
61. – 65.	0.076637	0.00150062	0.000474538	0.00229911
65. – 70.	0.0759462	0.00163643	0.000517484	0.00227839
70. – 75.	0.0734238	0.00154593	0.000488867	0.00220272
75. – 80.	0.0749548	0.0019587	0.000619396	0.00224864
80. – 85.	0.0728264	0.00160893	0.000508789	0.0021848
85. – 95.	0.0776449	0.00432023	0.00136618	0.00232935
95. – 105.	0.0722412	0.00178587	0.000564742	0.00216723
105. – 125.	0.0682163	0.00171466	0.000542224	0.00204649
125. – 150.	0.0606084	0.00219335	0.000693597	0.00181825
150. – 175.	0.0549135	0.00265379	0.000839202	0.00164741
175. – 200.	0.0500717	0.00341425	0.00107968	0.00150216
200. – 250.	0.0438294	0.00375023	0.00118593	0.0013149
250. – 300.	0.0255768	0.00730141	0.00230891	0.000767309
300. – 350.	0.0257082	0.00878564	0.00277826	0.000771414
350. – 400.	0.046506	0.0139431	0.00440919	0.00139526
400. – 470.	0.0257966	0.0160086	0.00506237	0.000774092
470. – 550.	0.0126944	0.0248429	0.007856	0.000380961
550. – 650.	0.00365842	0.0297732	0.00941513	0.000110922
650. – 900.	0.0541991	0.0472457	0.0149404	0.00162197
900. – 2500.	0.0367986	0.0994578	0.0314513	0.00110695

**Table 10:** Expected results of measurements of the  $A_2$  observable at the LHC at 13 TeV with 300 fb<sup>-1</sup> and 3 ab<sup>-1</sup>. The columns show the bin range, the expected value of  $A_2$ , the statistical uncertainty with 300 fb<sup>-1</sup> and 3 ab<sup>-1</sup>, and a systematic uncertainty of 3%.

$p_T^{\ell\ell}$ [GeV]	$A_0 - A_2$	$\delta(A_0 - A_2)_{\text{stat}}^{300}$	$\delta(A_0 - A_2)_{\text{stat}}^{3000}$	$\delta(A_0 - A_2)_{\text{syst}}^{3\%}$
10. – 12.	0.0283314	0.00219976	0.000695624	0.0186437
12. – 14.	0.0330746	0.002538	0.000802587	0.0182193
14. – 16.	0.0419759	0.00274345	0.000867555	0.0177411
16. – 18.	0.0415125	0.00280323	0.000886458	0.0172811
18. – 20.	0.0490277	0.00218055	0.000689551	0.0167469
20. – 22.5	0.0577262	0.00381117	0.0012052	0.0161526
22.5 – 25.	0.062618	0.00218661	0.000691467	0.0155138
25. – 27.5	0.0653363	0.00239468	0.000757264	0.0148491
27.5 – 30.	0.066978	0.00249069	0.000787625	0.0142801
30. – 33.	0.0764202	0.00216215	0.000683731	0.0136772
33. – 36.	0.0761219	0.00246108	0.000778261	0.0131836
36. – 39.	0.0853067	0.00485269	0.00153455	0.0127001
39. – 42.	0.0835377	0.00245159	0.000775261	0.0124663
42. – 45.	0.0908412	0.00268472	0.000848984	0.0122209
45. – 48.	0.0870325	0.00300801	0.000951216	0.0123383
48. – 51.	0.0925727	0.00348033	0.00110058	0.0123622
51. – 54.	0.089258	0.00357317	0.00112994	0.0126788
54. – 57.	0.0829	0.00435847	0.00137827	0.0131511
57. – 61.	0.094012	0.00298472	0.000943851	0.0133462
61. – 65.	0.0920686	0.00319159	0.00100927	0.0140083
65. – 70.	0.0915626	0.0031811	0.00100595	0.0146901
70. – 75.	0.0909227	0.0030153	0.000953521	0.0154339
75. – 80.	0.08731	0.00344346	0.00108892	0.0164048
80. – 85.	0.0913945	0.00421305	0.00133228	0.0171533
85. – 95.	0.0884333	0.00569044	0.00179947	0.0179584
95. – 105.	0.0861138	0.00424156	0.0013413	0.0194852
105. – 125.	0.0833509	0.00371347	0.0011743	0.0211513
125. – 150.	0.0839705	0.00447094	0.00141384	0.022989
150. – 175.	0.0834069	0.00632102	0.00199888	0.0242685
175. – 200.	0.0896245	0.00785136	0.00248282	0.0252912
200. – 250.	0.0792491	0.00902837	0.00285502	0.0262151
250. – 300.	0.0690518	0.0147523	0.0046651	0.0277607
300. – 350.	0.0671591	0.0205242	0.00649034	0.0277056
350. – 400.	0.07426	0.0326327	0.0103194	0.0286537
400. – 470.	0.0752987	0.0362228	0.0114547	0.0281729
470. – 550.	0.0679409	0.0490551	0.0155126	0.0292874
550. – 650.	0.0166015	0.0724604	0.022914	0.0307811
650. – 900.	0.142826	0.0871392	0.0275558	0.0267453
900. – 2500.	−0.109047	0.201254	0.063642	0.0343444

**Table 11:** Expected results of measurements of the  $A_0 - A_2$  observable at the LHC at 13 TeV with 300 fb<sup>−1</sup> and 3 ab<sup>−1</sup>. The columns show the bin range, the expected value of  $A_2$ , the statistical uncertainty with 300 fb<sup>−1</sup> and 3 ab<sup>−1</sup>, and a systematic uncertainty of 3%.

$m_{\ell\ell}$ [GeV]	$N_{\text{MC}}$	$\sigma$ [pb]	$\delta\sigma_{\text{stat}}^{300}$ [pb]	$\delta\sigma_{\text{stat}}^{3000}$ [pb]	$\delta\sigma_{\text{syst}}^{3\%}$ [pb]
100 – 105	8204433	18.1485	0.0118372	0.00374325	0.544455
105 – 110	8349055	8.82233	0.00550703	0.00174147	0.26467
110 – 115	7067831	5.25065	0.00322271	0.00101911	0.15752
115 – 120	7159110	3.50436	0.00213849	0.000676251	0.105131
120 – 126	5813465	2.94182	0.0020837	0.000658923	0.0882547
126 – 133	5797184	2.37394	0.00193485	0.000611855	0.0712182
133 – 141	3755474	1.95064	0.00176662	0.000558653	0.0585193
141 – 150	3813026	1.56363	0.00158484	0.00050117	0.046909
150 – 160	3096496	1.24575	0.00119425	0.000377655	0.0373726
160 – 171	3143515	0.992093	0.00101408	0.000320682	0.0297628
171 – 185	1601319	0.882853	0.00124199	0.000392753	0.0264856
185 – 200	1631284	0.669961	0.000768605	0.000243054	0.0200988
200 – 220	1662754	0.607422	0.000784724	0.000248151	0.0182227
220 – 243	1701384	0.454496	0.000570742	0.000180485	0.0136349
243 – 273	867442	0.368791	0.000635313	0.000200904	0.0110637
273 – 320	890247	0.3257	0.000636502	0.000201279	0.00977101
320 – 380	917527	0.201384	0.000397336	0.000125649	0.00604152
380 – 440	709781	0.100279	0.000218025	0.0000689457	0.00300837
440 – 510	361260	0.0603857	0.000172991	0.0000547046	0.00181157
510 – 600	370583	0.0400292	0.000123339	0.0000390033	0.00120088
600 – 700	380320	0.0211948	0.0000512655	0.0000162116	0.000635844
700 – 830	155170	0.0127793	0.0000579316	0.0000183196	0.000383379
830 – 1000	158533	0.00713393	0.0000317332	0.0000100349	0.000214018
1000 – 1500	162895	0.00501588	0.0000223981	$7.1 \cdot 10^{-6}$	0.000150477
1500 – 3000	166879	0.000848871	$5.0 \cdot 10^{-6}$	$1.6 \cdot 10^{-6}$	0.0000254661
3000 – 10000	2710	$9.5 \cdot 10^{-6}$	$1.1 \cdot 10^{-6}$	$3.4 \cdot 10^{-7}$	$2.9 \cdot 10^{-7}$

**Table 12:** Expected results of measurements of the di-lepton invariant mass spectrum at the LHC at 13 TeV with  $300 \text{ fb}^{-1}$  and  $3 \text{ ab}^{-1}$ . The columns show the bin range, the number of Monte Carlo events, the expected cross-section, the statistical uncertainty with  $300 \text{ fb}^{-1}$  and  $3 \text{ ab}^{-1}$ , and a systematic uncertainty of 3%.

$m_{\ell\ell}$ [GeV]	$A_0$	$(\delta A_0)_{\text{stat}}^{300}$	$(\delta A_0)_{\text{stat}}^{3000}$	$(\delta A_0)_{\text{syst}}^{3\%}$
100 – 105	0.206069	0.00220099	0.000696013	0.0138179
105 – 110	0.198655	0.00390891	0.0012361	0.0140404
110 – 115	0.192236	0.0043067	0.0013619	0.0142329
115 – 120	0.18408	0.00459632	0.00145349	0.0144776
120 – 126	0.178093	0.00527618	0.00166847	0.0146572
126 – 133	0.16969	0.00676013	0.00213774	0.0149093
133 – 141	0.163594	0.00667648	0.00211129	0.0150922
141 – 150	0.157821	0.00815895	0.00258008	0.0152653
150 – 160	0.150422	0.0090537	0.00286303	0.0154873
160 – 171	0.145611	0.0109549	0.00346424	0.0156316
171 – 185	0.137872	0.00920768	0.00291172	0.0158639
185 – 200	0.126617	0.0122699	0.00388007	0.0162015
200 – 220	0.124962	0.0136978	0.00433163	0.0162512
220 – 243	0.106773	0.0130855	0.00413799	0.0167968
243 – 273	0.0990207	0.0193292	0.00611242	0.0170294
273 – 320	0.097449	0.0197648	0.00625017	0.0170767
320 – 380	0.0809004	0.0236554	0.00748048	0.017573
380 – 440	0.0768314	0.0331067	0.0104693	0.0176951
440 – 510	0.0528575	0.0400658	0.0126699	0.0184143
510 – 600	0.0517298	0.0535121	0.016922	0.018448
600 – 700	0.0508636	0.0685334	0.0216721	0.0184748
700 – 830	0.0460793	0.0885335	0.0279967	0.0186168
830 – 1000	0.0420531	0.117322	0.0371003	0.0187368
1000 – 1500	0.0289552	0.141289	0.0446794	0.0191276
1500 – 3000	0.0236164	0.41192	0.130261	0.0192946
3000 – 10000	−0.673888	6.51047	2.05879	0.0415498

**Table 13:** Expected results of measurements of the  $A_0$  observable at the LHC at 13 TeV with 300 fb<sup>−1</sup> and 3 ab<sup>−1</sup>. The columns show the bin range, the expected value of  $A_0$ , the statistical uncertainty with 300 fb<sup>−1</sup> and 3 ab<sup>−1</sup>, and a systematic uncertainty of 3%.

$m_{\ell\ell}$ [GeV]	$A_2$	$(\delta A_2)_{\text{stat}}^{300}$	$(\delta A_2)_{\text{stat}}^{3000}$	$(\delta A_2)_{\text{syst}}^{3\%}$
100 – 105	0.0422219	0.00227595	0.000719719	0.00126666
105 – 110	0.0434971	0.00376089	0.0011893	0.00130493
110 – 115	0.0417116	0.00381904	0.00120769	0.00125134
115 – 120	0.038442	0.00474009	0.00149895	0.00115326
120 – 126	0.0355266	0.00459244	0.00145226	0.0010658
126 – 133	0.0373691	0.00624652	0.00197532	0.00112104
133 – 141	0.0345992	0.00571451	0.00180709	0.00103799
141 – 150	0.0364752	0.0083864	0.00265201	0.00109429
150 – 160	0.0364136	0.00710229	0.00224594	0.00109239
160 – 171	0.0291341	0.00948309	0.00299882	0.000874032
171 – 185	0.0356255	0.0085101	0.00269113	0.0010688
185 – 200	0.019759	0.0103417	0.00327033	0.000592756
200 – 220	0.0294363	0.0106759	0.00337601	0.000883093
220 – 243	0.0237177	0.0105273	0.00332902	0.000711509
243 – 273	0.0167273	0.0144559	0.00457135	0.000501912
273 – 320	0.0221835	0.0139955	0.00442577	0.000665533
320 – 380	0.0170735	0.0210878	0.00666854	0.000512299
380 – 440	0.0149437	0.0288257	0.00911549	0.00044819
440 – 510	0.00187905	0.0365037	0.0115435	0.0000557831
510 – 600	−0.00137813	0.0457439	0.0144655	0.0000413211
600 – 700	−0.00159732	0.0612091	0.019356	0.0000482714
700 – 830	−0.00557428	0.0672415	0.0212636	0.000167436
830 – 1000	0.0137169	0.10256	0.0324322	0.000410183
1000 – 1500	0.0317234	0.122617	0.038775	0.000951331
1500 – 3000	−0.00716862	0.396067	0.125248	0.000207753
3000 – 10000	2.86876	20.4434	6.46477	0.0919646

**Table 14:** Expected results of measurements of the  $A_2$  observable at the LHC at 13 TeV with 300 fb<sup>−1</sup> and 3 ab<sup>−1</sup>. The columns show the bin range, the expected value of  $A_2$ , the statistical uncertainty with 300 fb<sup>−1</sup> and 3 ab<sup>−1</sup>, and a systematic uncertainty of 3%.



$m_{\ell\ell}$ [GeV]	$A_0 - A_2$	$\delta(A_0 - A_2)_{\text{stat}}^{300}$	$\delta(A_0 - A_2)_{\text{stat}}^{3000}$	$\delta(A_0 - A_2)_{\text{syst}}^{3\%}$
100 – 105	0.0489227	0.00379057	0.00119868	0.0146
105 – 110	0.0479573	0.00693351	0.00219257	0.0147503
110 – 115	0.0527973	0.00846707	0.00267752	0.0148349
115 – 120	0.0466155	0.00778599	0.00246215	0.0150535
120 – 126	0.0443988	0.0108978	0.0034462	0.0151961
126 – 133	0.0483033	0.0123165	0.00389482	0.0153476
133 – 141	0.0355806	0.0115509	0.00365273	0.0155731
141 – 150	0.0366276	0.0141871	0.00448637	0.0156924
150 – 160	0.0365152	0.0167127	0.00528503	0.0158598
160 – 171	0.0364686	0.0246929	0.00780859	0.0159708
171 – 185	0.0487894	0.0189455	0.00599109	0.0160874
185 – 200	0.0310485	0.0205385	0.00649484	0.0164532
200 – 220	0.0324652	0.0236061	0.00746492	0.0164864
220 – 243	0.0265552	0.0210694	0.00666273	0.0169683
243 – 273	0.0127414	0.0364795	0.0115358	0.0172249
273 – 320	0.039359	0.0307471	0.00972308	0.0171653
320 – 380	0.0332408	0.0434818	0.0137501	0.0176311
380 – 440	0.0179427	0.0558835	0.0176719	0.017783
440 – 510	−0.0132197	0.080222	0.0253684	0.0185206
510 – 600	0.0147696	0.1048	0.0331407	0.0184813
600 – 700	0.0223771	0.134543	0.0425464	0.0184946
700 – 830	−0.0145346	0.174328	0.0551275	0.0187056
830 – 1000	0.0364093	0.226636	0.0716687	0.0187375
1000 – 1500	−0.0000212533	0.269824	0.0853259	0.0191475
1500 – 3000	0.0905146	0.904677	0.286084	0.0193981
3000 – 10000	3.38865	37.2917	11.7927	0.146803

**Table 15:** Expected results of measurements of the  $A_0 - A_2$  observable at the LHC at 13 TeV with 300  $\text{fb}^{-1}$  and 3  $\text{ab}^{-1}$ . The columns show the bin range, the expected value of  $A_0 - A_2$ , the statistical uncertainty with 300  $\text{fb}^{-1}$  and 3  $\text{ab}^{-1}$ , and a systematic uncertainty of 3%.

## F UV models sensitive to our analysis

One of the goals of the SMEFT program is that of indirectly exploring the landscape of possible UV completions of the SM. Generally, this is done by constraining, through precision measurements, the Wilson coefficients of classes of SMEFT operators, and then match them to a specific BSM model, or, even better, to a class of BSM models. Indeed, it is essential to keep in mind that the SMEFT approach, being fully model-independent, gives little information on the UV, unless it is supplemented by additional hypotheses. For instance, constraints on electroweak precision observables give very different information on the UV if one assumes strongly interacting dynamics at the TeV scale, or weakly coupled extensions of the SM. In other words, the SMEFT gains all its power only when supplemented by reasonable hypotheses at least on the BSM framework that can give rise to the observables at hand.

An interesting question that one could ask on the present paper is which information on the UV one could gather from studying the operators that we consider. First of all, the fact that dipole and scalar/tensor four-fermion operators break chiral symmetry, rules out the possibility of leveraging our analysis to constrain minimal flavor violating (MFV) UV models. Indeed, if MFV is assumed, then selection rules imply that the Wilson coefficients of chirality-breaking operators are suppressed by (powers of) Yukawa couplings, making our bounds too weak to draw any relevant conclusion. Parity is the other selection rule that makes all constraints on parity-odd operators, both four-fermion and dipole operators, the latter corresponding to Electric Dipole Moments (EDMs) from high energy measurements essentially irrelevant. This is the reason why we considered only parity conserving operators. Concerning parity conserving dipole operators, corresponding to Magnetic Dipole Moments (MDMs), the impact of UV physics is quite well understood, since they often arise from one loop diagrams that contribute to the  $U(1)_Y$ ,  $SU(2)_L$  and  $SU(3)_c$  vertex correction, to which there is usually a limited set of contributing Feynman diagrams. The general structure of these operators is therefore relatively easy to understand. For instance, Ref. [54] studies the one-loop contributions to dipole moments in several UV theories, such as two-Higgs-doublet models, the minimal supersymmetric extension of the SM (MSSM), and scenarios with extra  $U(1)$  gauge symmetries, and performs the matching with the SMEFT operators that we consider: the general result is that, within the framework of the aforementioned BSM theories, suitable parameter choices can lead to sizable Wilson coefficients for the CP-even dipole operators. These parameter choices are often fine-tuned, which is expected for sizeable chirality breaking contributions, but are still possible. In this respect, our bounds can be used to constrain such parameter choices, and to limit the possible fine-tuning available in some of these BSM scenarios.

Let us now briefly discuss four-fermion operators. As discussed, for instance, in Refs. [55, 56], they can be generated at tree level in BSM models which include leptoquark states. In particular the operators  $Q_{\ell equ}^{(1)}$  and  $Q_{\ell equ}^{(3)}$  can be generated by integrating out at tree level scalar leptoquarks, while  $Q_{\ell edq}$  can be generated by integrating out at tree-level vector leptoquarks. Notice that, because of their chiral structure, the operators  $Q_{\ell edq}$  and  $Q_{\ell equ}^{(1)}$  introduce terms in the pion decay width  $\Gamma(\pi \rightarrow \ell \nu_\ell)$  that are proportional

to the pion mass [57]. In particular, one finds that the ratio between the SM and the NP contribution scales as

$$\frac{\Gamma(\pi^+ \rightarrow \ell^+ \nu_\ell)^{\text{SM}}}{\Gamma(\pi^+ \rightarrow \ell^+ \nu_\ell)^{\text{NP}}} \propto \frac{m_\pi^2}{m_\ell(m_d + m_u)}. \quad (\text{F.1})$$

This contribution is reasonable for the muon channel, but it is hugely enhanced for the electron channel. As a consequence, one can check that for  $\Lambda$  of  $\mathcal{O}(1 \text{ TeV})$ , the present experimental measurement of the ratio [58]

$$R \equiv \frac{\Gamma(\pi^+ \rightarrow e^+ \nu_e)}{\Gamma(\pi^+ \rightarrow \mu^+ \nu_\mu)} = (1.230 \pm 0.004) \times 10^{-4}, \quad (\text{F.2})$$

implies, for the electron channel,  $c_{ledq} + c_{lequ}^{(1)} \sim \mathcal{O}(10^{-4})$ .<sup>15</sup> For this reason, as already mentioned in the main text, our bounds on the  $Q_{ledq}$  and  $Q_{lequ}^{(1)}$  operators are only relevant for the second family.

---

<sup>15</sup>This was also pointed out in Refs. [59, 60].

## References

- [1] C. Duhr, F. Dulat and B. Mistlberger, “*Drell-Yan Cross Section to Third Order in the Strong Coupling Constant*”, *Phys. Rev. Lett.* **125** (2020) 172001, [arXiv:2001.07717](#) [INSPIRE] [SEMANTIC SCHOLAR].
- [2] X. Chen, T. Gehrmann, N. Glover, A. Huss, T.-Z. Yang and H. X. Zhu, “*Dilepton Rapidity Distribution in Drell-Yan Production to Third Order in QCD*”, *Phys. Rev. Lett.* **128** (2022) 052001, [arXiv:2107.09085](#) [INSPIRE] [SEMANTIC SCHOLAR].
- [3] C. Duhr, F. Dulat and B. Mistlberger, “*Charged current Drell-Yan production at  $N^3LO$* ”, *JHEP* **11** (2020) 143, [arXiv:2007.13313](#) [INSPIRE] [SEMANTIC SCHOLAR].
- [4] C. Duhr and B. Mistlberger, “*Lepton-pair production at hadron colliders at  $N^3LO$  in QCD*”, *JHEP* **03** (2022) 116, [arXiv:2111.10379](#) [INSPIRE] [SEMANTIC SCHOLAR].
- [5] T. Armadillo, R. Bonciani, S. Devoto, N. Rana and A. Vicini, “*Two-loop mixed QCD-EW corrections to neutral current Drell-Yan*”, *JHEP* **05** (2022) 072, [arXiv:2201.01754](#) [INSPIRE] [SEMANTIC SCHOLAR].
- [6] R. Bonciani, L. Buonocore, M. Grazzini, S. Kallweit, N. Rana, F. Tramontano et al., “*Mixed Strong-Electroweak Corrections to the Drell-Yan Process*”, *Phys. Rev. Lett.* **128** (2022) 012002, [arXiv:2106.11953](#) [INSPIRE] [SEMANTIC SCHOLAR].
- [7] T. Armadillo, R. Bonciani, L. Buonocore, S. Devoto, M. Grazzini, S. Kallweit et al., “*Mixed QCD-EW corrections to the neutral-current Drell-Yan process*”, *JHEP* **07** (2025) 141, [arXiv:2412.16095](#) [INSPIRE] [SEMANTIC SCHOLAR].
- [8] M. Farina, G. Panico, D. Pappadopulo, J. T. Ruderman, R. Torre and A. Wulzer, “*Energy helps accuracy: electroweak precision tests at hadron colliders*”, *Phys. Lett. B* **772** (2017) 210, [arXiv:1609.08157](#) [INSPIRE] [SEMANTIC SCHOLAR].
- [9] X. Li, B. Yan and C. P. Yuan, “*Lam-Tung relation breaking in Z boson production as a probe of standard model effective field theory effects*”, *Phys. Rev. D* **111** (2025) 073007, [arXiv:2405.04069](#) [INSPIRE] [SEMANTIC SCHOLAR].
- [10] B. Grzadkowski, M. Iskrzynski, M. Misiak and J. Rosiek, “*Dimension-Six Terms in the Standard Model Lagrangian*”, *JHEP* **10** (2010) 085, [arXiv:1008.4884](#) [INSPIRE] [SEMANTIC SCHOLAR].
- [11] R. Torre, L. Ricci and A. Wulzer, “*On the  $W\ell Y$  interpretation of high-energy Drell-Yan measurements*”, *JHEP* **02** (2021) 144, [arXiv:2008.12978](#) [INSPIRE] [SEMANTIC SCHOLAR].
- [12] G. Panico, L. Ricci and A. Wulzer, “*High-energy EFT probes with fully differential Drell-Yan measurements*”, *JHEP* **07** (2021) 086, [arXiv:2103.10532](#) [INSPIRE] [SEMANTIC SCHOLAR].
- [13] S. Grossi and R. Torre, “*More variables or more bins? Impact on the EFT interpretation of Drell-Yan measurements*”, *Eur. Phys. J. C* **84** (2024) 713, [arXiv:2404.10569](#) [INSPIRE] [SEMANTIC SCHOLAR].
- [14] T. Corbett, J. Desai, O. J. P. Eboli, M. C. Gonzalez-Garcia, M. Martinez and P. Reimitz, “*Drell-Yan production in universal theories beyond dimension-six SMEFT*”, *Phys. Rev. D* **112** (2025) 013009, [arXiv:2503.19962](#) [INSPIRE] [SEMANTIC SCHOLAR].
- [15] C. S. Lam and W.-K. Tung, “*A Systematic Approach to Inclusive Lepton Pair Production in Hadronic Collisions*”, *Phys. Rev. D* **18** (1978) 2447 [INSPIRE] [SEMANTIC SCHOLAR].

- [16] C. S. Lam and W.-K. Tung, “Structure Function Relations at Large Transverse Momenta in Lepton Pair Production Processes”, *Phys. Lett. B* **80** (1979) 228 [INSPIRE] [SEMANTIC SCHOLAR].
- [17] J. C. Collins and D. E. Soper, “Angular Distribution of Dileptons in High-Energy Hadron Collisions”, *Phys. Rev. D* **16** (1977) 2219 [INSPIRE] [SEMANTIC SCHOLAR].
- [18] G. Li, X. Li and B. Yan, “Lam-Tung relation breaking effects and weak dipole moments at lepton colliders”, *Phys. Lett. B* **870** (2025) 139931, [arXiv:2503.17663](#) [INSPIRE] [SEMANTIC SCHOLAR].
- [19] R. Gauld, U. Haisch and J. Weiss, “A tale of  $Z$ +jet: SMEFT effects and the Lam-Tung relation”, *SciPost Phys.* **18** (2025) 148, [arXiv:2412.13014](#) [INSPIRE] [SEMANTIC SCHOLAR].
- [20] V. E. Lyubovitskij, A. S. Zhevlakov and I. A. Anikin, “Angular coefficients of the Drell-Yan process across different rapidity and kinematical ranges”, *Phys. Rev. D* **112** (2025) 054023, [arXiv:2503.16008](#) [INSPIRE] [SEMANTIC SCHOLAR].
- [21] Y. B. Bandeira, V. P. Goncalves and W. Schäfer, “Dilepton angular distributions in the color-dipole  $S$ -matrix framework”, *JHEP* **10** (2025) 010, [arXiv:2507.06207](#) [INSPIRE] [SEMANTIC SCHOLAR].
- [22] F. Petriello and K. Şimşek, “Naive  $T$ -odd Drell-Yan angular coefficients as a probe of the dimension-8 SMEFT”, , [arXiv:2511.19617](#) [INSPIRE] [SEMANTIC SCHOLAR].
- [23] P. F. Monni, P. Nason, E. Re, M. Wiesemann and G. Zanderighi, “ $MiNNLO_{PS}$ : a new method to match NNLO QCD to parton showers”, *JHEP* **05** (2020) 143, [arXiv:1908.06987](#) [INSPIRE] [SEMANTIC SCHOLAR].
- [24] P. F. Monni, E. Re and M. Wiesemann, “ $MiNNLO_{PS}$ : optimizing  $2 \rightarrow 1$  hadronic processes”, *Eur. Phys. J. C* **80** (2020) 1075, [arXiv:2006.04133](#) [INSPIRE] [SEMANTIC SCHOLAR].
- [25] P. Nason, “A New method for combining NLO QCD with shower Monte Carlo algorithms”, *JHEP* **11** (2004) 040, [hep-ph/0409146](#) [INSPIRE] [SEMANTIC SCHOLAR].
- [26] S. Frixione, P. Nason and C. Oleari, “Matching NLO QCD computations with Parton Shower simulations: the POWHEG method”, *JHEP* **11** (2007) 070, [arXiv:0709.2092](#) [INSPIRE] [SEMANTIC SCHOLAR].
- [27] S. Alioli, P. Nason, C. Oleari and E. Re, “A general framework for implementing NLO calculations in shower Monte Carlo programs: the POWHEG BOX”, *JHEP* **06** (2010) 043, [arXiv:1002.2581](#) [INSPIRE] [SEMANTIC SCHOLAR].
- [28] T. Sjöstrand, S. Mrenna and P. Z. Skands, “A Brief Introduction to PYTHIA 8.1”, *Comput. Phys. Commun.* **178** (2008) 852, [arXiv:0710.3820](#) [INSPIRE] [SEMANTIC SCHOLAR].
- [29] T. Sjöstrand, S. Ask, J. R. Christiansen, R. Corke, N. Desai, P. Ilten et al., “An introduction to PYTHIA 8.2”, *Comput. Phys. Commun.* **191** (2015) 159, [arXiv:1410.3012](#) [INSPIRE] [SEMANTIC SCHOLAR].
- [30] C. Bierlich et al., “A comprehensive guide to the physics and usage of PYTHIA 8.3”, *SciPost Phys. Codeb.* **2022** (2022) 8, [arXiv:2203.11601](#) [INSPIRE] [SEMANTIC SCHOLAR].
- [31] J. Alwall et al., “A Standard format for Les Houches event files”, *Comput. Phys. Commun.* **176** (2007) 300, [hep-ph/0609017](#) [INSPIRE] [SEMANTIC SCHOLAR].
- [32] V. Shtabovenko, R. Mertig and F. Orellana, “FeynCalc 9.3: New features and

- improvements”, *Comput. Phys. Commun.* **256** (2020) 107478, [arXiv:2001.04407](#) [INSPIRE] [SEMANTIC SCHOLAR].
- [33] T. Hahn, “Generating Feynman diagrams and amplitudes with FeynArts 3”, *Comput. Phys. Commun.* **140** (2001) 418, [hep-ph/0012260](#) [INSPIRE] [SEMANTIC SCHOLAR].
- [34] Wolfram Research, Inc., Mathematica, Version 13.0 Champaign, IL, 2021 [WEBSITE].
- [35] D. B. Clark, E. Godat and F. I. Olness, “ManeParse : A Mathematica reader for Parton Distribution Functions”, *Comput. Phys. Commun.* **216** (2017) 126, [arXiv:1605.08012](#) [INSPIRE] [SEMANTIC SCHOLAR].
- [36] A. Buckley, J. Ferrando, S. Lloyd, K. Nordström, B. Page, M. Rüfenacht et al., “LHAPDF6: parton density access in the LHC precision era”, *Eur. Phys. J. C* **75** (2015) 132, [arXiv:1412.7420](#) [INSPIRE] [SEMANTIC SCHOLAR].
- [37] ATLAS Collaboration, G. Aad et al., “Precise measurements of  $W$ - and  $Z$ -boson transverse momentum spectra with the ATLAS detector using  $pp$  collisions at  $\sqrt{s} = 5.02$  TeV and 13 TeV”, *Eur. Phys. J. C* **84** (2024) 1126, [arXiv:2404.06204](#) [INSPIRE] [SEMANTIC SCHOLAR].
- [38] ATLAS Collaboration, G. Aad et al., “A precise measurement of the  $Z$ -boson double-differential transverse momentum and rapidity distributions in the full phase space of the decay leptons with the ATLAS experiment at  $\sqrt{s} = 8$  TeV”, *Eur. Phys. J. C* **84** (2024) 315, [arXiv:2309.09318](#) [INSPIRE] [SEMANTIC SCHOLAR].
- [39] CMS Collaboration, A. Tumasyan et al., “Measurement of the mass dependence of the transverse momentum of lepton pairs in Drell-Yan production in proton-proton collisions at  $\sqrt{s} = 13$  TeV”, *Eur. Phys. J. C* **83** (2023) 628, [arXiv:2205.04897](#) [INSPIRE] [SEMANTIC SCHOLAR].
- [40] LHCb Collaboration, R. Aaij et al., “First Measurement of the  $Z \rightarrow \mu^+ \mu^-$  Angular Coefficients in the Forward Region of  $pp$  Collisions at  $s = 13$  TeV”, *Phys. Rev. Lett.* **129** (2022) 091801, [arXiv:2203.01602](#) [INSPIRE] [SEMANTIC SCHOLAR].
- [41] ATLAS Collaboration, G. Aad et al., “Measurement of the transverse momentum distribution of Drell-Yan lepton pairs in proton-proton collisions at  $\sqrt{s} = 13$  TeV with the ATLAS detector”, *Eur. Phys. J. C* **80** (2020) 616, [arXiv:1912.02844](#) [INSPIRE] [SEMANTIC SCHOLAR].
- [42] CMS Collaboration, A. M. Sirunyan et al., “Measurements of differential  $Z$  boson production cross sections in proton-proton collisions at  $\sqrt{s} = 13$  TeV”, *JHEP* **12** (2019) 061, [arXiv:1909.04133](#) [INSPIRE] [SEMANTIC SCHOLAR].
- [43] CMS Collaboration, A. M. Sirunyan et al., “Measurement of the differential Drell-Yan cross section in proton-proton collisions at  $\sqrt{s} = 13$  TeV”, *JHEP* **12** (2019) 059, [arXiv:1812.10529](#) [INSPIRE] [SEMANTIC SCHOLAR].
- [44] CMS Collaboration, A. M. Sirunyan et al., “Measurement of differential cross sections in the kinematic angular variable  $\phi^*$  for inclusive  $Z$  boson production in  $pp$  collisions at  $\sqrt{s} = 8$  TeV”, *JHEP* **03** (2018) 172, [arXiv:1710.07955](#) [INSPIRE] [SEMANTIC SCHOLAR].
- [45] ATLAS Collaboration, M. Aaboud et al., “Measurement of the Drell-Yan triple-differential cross section in  $pp$  collisions at  $\sqrt{s} = 8$  TeV”, *JHEP* **12** (2017) 059, [arXiv:1710.05167](#) [INSPIRE] [SEMANTIC SCHOLAR].
- [46] CMS Collaboration, V. Khachatryan et al., “Measurement of the transverse momentum

- spectra of weak vector bosons produced in proton-proton collisions at  $\sqrt{s} = 8 \text{ TeV}$ ", *JHEP* **02** (2017) 096, [arXiv:1606.05864](#) [INSPIRE] [SEMANTIC SCHOLAR].
- [47] **ATLAS** Collaboration, G. Aad et al., "Measurement of the double-differential high-mass Drell-Yan cross section in  $pp$  collisions at  $\sqrt{s} = 8 \text{ TeV}$  with the ATLAS detector", *JHEP* **08** (2016) 009, [arXiv:1606.01736](#) [INSPIRE] [SEMANTIC SCHOLAR].
- [48] **ATLAS** Collaboration, G. Aad et al., "Measurement of the angular coefficients in  $Z$ -boson events using electron and muon pairs from data taken at  $\sqrt{s} = 8 \text{ TeV}$  with the ATLAS detector", *JHEP* **08** (2016) 159, [arXiv:1606.00689](#) [INSPIRE] [SEMANTIC SCHOLAR].
- [49] **ATLAS** Collaboration, G. Aad et al., "Measurement of the transverse momentum and  $\phi_\eta^*$  distributions of Drell-Yan lepton pairs in proton-proton collisions at  $\sqrt{s} = 8 \text{ TeV}$  with the ATLAS detector", *Eur. Phys. J. C* **76** (2016) 291, [arXiv:1512.02192](#) [INSPIRE] [SEMANTIC SCHOLAR].
- [50] **CMS** Collaboration, V. Khachatryan et al., "Angular coefficients of  $Z$  bosons produced in  $pp$  collisions at  $\sqrt{s} = 8 \text{ TeV}$  and decaying to  $\mu^+\mu^-$  as a function of transverse momentum and rapidity", *Phys. Lett. B* **750** (2015) 154, [arXiv:1504.03512](#) [INSPIRE] [SEMANTIC SCHOLAR].
- [51] **CMS** Collaboration, V. Khachatryan et al., "Measurement of the  $Z$  boson differential cross section in transverse momentum and rapidity in proton-proton collisions at  $8 \text{ TeV}$ ", *Phys. Lett. B* **749** (2015) 187, [arXiv:1504.03511](#) [INSPIRE] [SEMANTIC SCHOLAR].
- [52] N. Arteaga-Romero, A. Nicolaidis and J. Silva, " $Z^0$  Production at the  $p\bar{p}$  Collider and the Spin of the Gluon", *Phys. Rev. Lett.* **52** (1984) 172 [INSPIRE] [SEMANTIC SCHOLAR].
- [53] J. Alwall, M. Herquet, F. Maltoni, O. Mattelaer and T. Stelzer, "MadGraph 5: Going Beyond", *JHEP* **06** (2011) 128, [arXiv:1106.0522](#) [INSPIRE] [SEMANTIC SCHOLAR].
- [54] N. Valori and O. Vives, "Beyond the Standard Model contributions to dipole moments", , [arXiv:2505.06345](#) [INSPIRE] [SEMANTIC SCHOLAR].
- [55] J. de Blas, J. C. Criado, M. Perez-Victoria and J. Santiago, "Effective description of general extensions of the Standard Model: the complete tree-level dictionary", *JHEP* **03** (2018) 109, [arXiv:1711.10391](#) [INSPIRE] [SEMANTIC SCHOLAR].
- [56] I. Doršner, S. Fajfer, A. Greljo, J. F. Kamenik and N. Košnik, "Physics of leptoquarks in precision experiments and at particle colliders", *Phys. Rept.* **641** (2016) 1, [arXiv:1603.04993](#) [INSPIRE] [SEMANTIC SCHOLAR].
- [57] O. U. Shanker, " $\pi\ell$  2,  $K\ell$  3 and  $K^0 - \bar{K}^0$  Constraints on Leptoquarks and Supersymmetric Particles", *Nucl. Phys. B* **204** (1982) 375 [INSPIRE] [SEMANTIC SCHOLAR].
- [58] **Particle Data Group** Collaboration, S. Navas et al., "Review of particle physics", *Phys. Rev. D* **110** (2024) 030001 [INSPIRE].
- [59] M. Leurer, "A Comprehensive study of leptoquark bounds", *Phys. Rev. D* **49** (1994) 333, [hep-ph/9309266](#) [INSPIRE] [SEMANTIC SCHOLAR].
- [60] M. Leurer, "Bounds on vector leptoquarks", *Phys. Rev. D* **50** (1994) 536, [hep-ph/9312341](#) [INSPIRE] [SEMANTIC SCHOLAR].